Peer reviewed version of the manuscript published in final form at ACS Nano, 2019,
DOI:10.1021/acsnano.8b06492.

Bio-Inspired Fabrication of DNA-Inorganic Hybrid Composites Using Synthetic DNA

Eunjung Kim,[1] Shweta Agarwal,[1] Nayoung Kim,[1] Fredrik Sydow Hage,[2] Vincent Leonardo,[1] Amy Gelmi,[1] and Molly M. Stevens[1]*

[1]Department of Materials, Department of Bioengineering and Institute for Biomedical Engineering, Imperial College London, London, SW7 2AZ, United Kingdom

[2]SuperSTEM Laboratory, SciTech Daresbury Campus, Daresbury WA4 4AD, United Kingdom

Correspondence to:

*Email: m.stevens@imperial.ac.uk

Peer reviewed version of the manuscript published in final form at ACS Nano, 2019,
DOI:10.1021/acsnano.8b06492.

ABSTRACT

Nucleic acid nanostructures have attracted significant interest as potential therapeutic and diagnostic platforms due to their intrinsic biocompatibility and biodegradability, structural and functional diversity, and compatibility with various chemistries for modification and stabilization. Among the fabrication approaches for such structures, the rolling circle techniques have emerged as particularly promising, producing morphologically round, flower-shaped nucleic acid particles: typically hybrid composites of long nucleic acid strands and inorganic magnesium pyrophosphate (Mg_2PPi). These constructs are known to form *via* anisotropic nucleic acid-driven crystallization in a sequence-independent manner, rendering monodisperse and densely packed RNA or DNA-inorganic composites. However, it still remains to fully explore how flexible polymer-like RNA or DNA strands (acting as biomolecular additives) mediate the crystallization process of Mg_2PPi and affect the structure and properties of the product crystals. To address this, we closely examined nanoscale details to mesoscopic features of Mg_2PPi/DNA hybrid composites fabricated by two approaches, namely rolling circle amplification (RCA)-based *in situ* synthesis and long synthetic DNA-mediated crystallization. Similar to the DNA constructs fabricated by RCA, the rapid crystallization of Mg_2PPi was retarded on a short-range order when we precipitated the crystals in the presence of pre-synthesized long DNA, which resulted in effective incorporation of biomolecular additives such as DNA and enzymes. These findings further provide a more feasible way to encapsulate bioactive enzymes within DNA constructs compared to *in situ* RCA-mediated synthesis: *i.e.* by not only protecting them from possible denaturation under the reaction conditions but also preventing non-selective association of proteins arising from the RCA reaction mixtures.

Peer reviewed version of the manuscript published in final form at ACS Nano, 2019,
DOI:10.1021/acsnano.8b06492.

KEYWORDS: DNA-inorganic hybrid composites, rolling circle techniques, crystallization, co-precipitation, DNA inclusion

Biomimetic crystallization methods have been exploited to build functional materials with a variety of specialized and complex properties similar to naturally occurring biominerals.[1,2] Such methods involve homogeneous or heterogeneous nucleation and growth of organic and inorganic phases in materials, inducing highly ordered, hierarchical structures with well-defined morphologies, sizes, and polymorphs.[2,3] In such a way, one can generate DNA-inorganic hybrid composites mainly composed of DNA and magnesium pyrophosphate (Mg_2PPi), generated by rolling circle techniques such as rolling circle amplification (RCA) or transcription (RCT) based on isothermal enzymatic polymerization.[4,5] In contrast to DNA nanostructures assembled by Watson-Crick base pairing, they form morphologically spherical, flower-like nucleic acid particles through *in situ* nucleic acid-driven crystallization of metal salts (here Mg_2PPi) generated during the reaction.[5-8] Due to their large surface areas and highly porous structures, coupled with intrinsic DNA and RNA properties and functionalities, these RCA or RCT-based nano/microparticles are of utility for biomedical applications.[4-6,8-15] However, further study is needed on how the presence of long DNA or RNA as organic additives and structure-directing agents – whether they are *in situ* synthesized or pre-synthesized – can modulate the Mg_2PPi crystal growth and direct the outcome structures of particles during the RCA or RCT process.

Indeed, there is a lack of reports showing how the Mg_2PPi crystals evolve chemically and morphologically by the introduction of DNA or RNA molecules during the reaction. While Shopsowitz *et al.* demonstrated that addition of RNA into a certain concentration of Mg_2PPi dramatically changed the particle morphology compared to that without RNA,[7] more substantial

Peer reviewed version of the manuscript published in final form at ACS Nano, 2019,
DOI:10.1021/acsnano.8b06492.

evidence is required to fully understand the role of the produced RNA molecules during the RCT process. Apart from the typical RCA-based fabrication of DNA particles, various RCA-inspired approaches have been recently proposed by focusing more on the critical role of divalent cations in controlling size, morphology, and functionality of the resulting DNA particles.[16-18] These approaches present an effective route for preparation of functional DNA-inorganic hybrid particles. However, studying how the inclusion of long DNA serving as organic additives in Mg_2PPi crystal growth affects the molecular interaction between DNA and inorganic crystals still remains unexplored. These organic macromolecules appear to be intimately associated with the Mg_2PPi phase through mainly electrostatic interaction in common with RCA-driven *in situ* formation of DNA particles, where multiple interactions occur between growing DNA and Mg_2PPi over time.

Moreover, the majority of characterizations of RCA- or RCT-based particles have so far focused on their surface morphology, composition, and size using scanning and transmission electron microscopy (SEM and TEM). In terms of nanostructural investigation, multimodal coherent X-ray diffraction analysis of RCT-mediated RNA microparticles (termed RNAi microsponges) recently revealed the existence of a dense internal core region within the particles.[19] This technique allows for two- and three-dimensional electron density imaging of such biological materials at the nano-scale. However, this method does not provide detailed hemical and atomic information that would demonstrate molecular relationships between organic and inorganic matter within the RNAi microsponges.

Here, we studied and identified the differences in the nanostructural morphology, chemical composition, atomic bonding configuration, and crystallinity of various Mg_2PPi/DNA composites prepared by two RCA-inspired approaches. We used various advanced

Peer reviewed version of the manuscript published in final form at ACS Nano, 2019,
DOI:10.1021/acsnano.8b06492.

characterization methods, including high-resolution scanning transmission electron microscopy (STEM) imaging in combination with energy dispersive X-ray spectroscopy (EDS) and electron energy loss spectroscopy (EELS), X-ray diffraction (XRD), and Raman spectroscopy.

RESULTS AND DISCUSSION

Motivated by our previous study,[8] we further question how pre-synthesized long DNA (specifically isolated from the RCA) can affect the structure and chemical pathways controlling the organization process of Mg_2PPi crystals in comparison to *in situ* synthesized DNA-driven Mg_2PPi growth. To address this, we designed two strategies for fabrication of Mg_2PPi/DNA hybrid composites based on: (1) *in situ* RCA-driven synthesis and (2) a synthetic DNA-directed crystallization method (Scheme 1). During the *in situ* synthesis, continuously growing DNA strands and Mg_2PPi crystals formed hierarchical, flower-shaped DNA structures (termed DNF hereafter) for the desired reaction time (20 h in this study). On the other hand, in the synthetic DNA-driven crystallization method, first we solely isolated the amplified DNA (AmpDNA) from the products after 20 h RCA in the presence of inorganic pyrophosphatase (PPase) through subsequent purification by ethanol precipitation. After removal of salts and proteins, the resulting AmpDNA was then precipitated out in a neutral buffer containing concentrated Mg and PPi ions (for 20 h) in order to produce another class of DNA-inorganic hybrid composites (termed Mg_2PPi/AmpDNA hereafter).

In the RCA reaction, the phi29 DNA polymerase (φ29 DNAP) simultaneously produces DNA strands and pyrophosphate (PPi^{4-}) ions in a time-dependent manner.[8] The released anionic PPi ions tend to form insoluble Mg_2PPi precipitates with cationic magnesium (Mg^{2+}) ions supplied from the reaction buffer when they reach a sufficient concentration. On the other hand, the

Peer reviewed version of the manuscript published in final form at ACS Nano, 2019,
DOI:10.1021/acsnano.8b06492.

addition of PPase to the RCA reaction mixtures converts PPi to phosphate (Pi) ions and inhibits the formation of Mg_2PPi precipitates. As a result, long DNA strands are produced rather than DNA particles. The released Pi ions may also be involved in the formation of magnesium hydrogen phosphate (MgHPi) complexes, which are partially soluble in aqueous solution. In addition to MgHPi, several ionic species and complexes, including free Mg ions, PPi ions, MgPPi ions, MgHPPi ions, Mg_2PPi, *etc.*, may present in the initial RCA reaction mixture or be produced as the reaction proceeds.[20] However, it is important to note that when adding PPase, we did not observe any precipitates or particles remaining after the RCA reaction and several washing steps, possibly due to the low amount of those complexes present in reaction solution being below the solubility limit (data not shown).

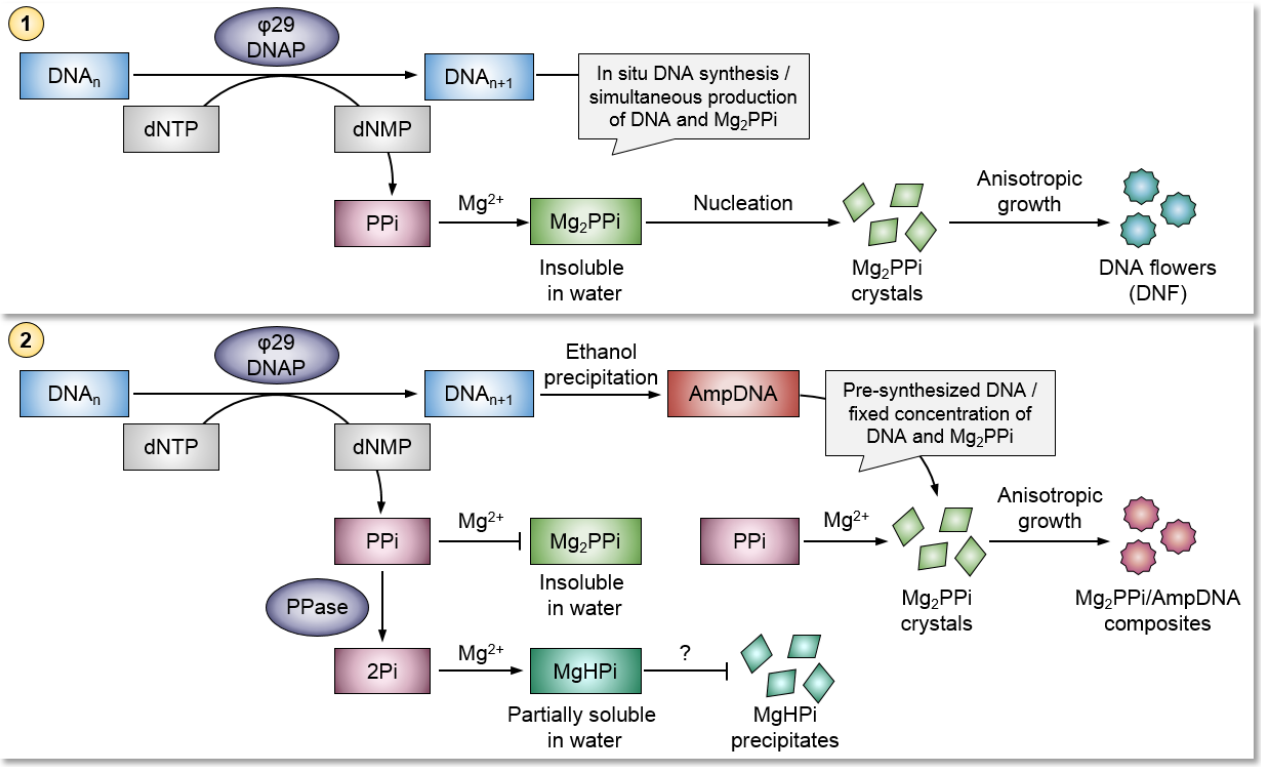

Scheme 1. Overview of the fabrication of DNA-inorganic hybrid composites. 1) DNA flowers (DNF) constructed by one-pot enzymatic process using rolling circle amplification (RCA) and 2) Mg_2PPi/AmpDNA composites formed by synthetic DNA-driven crystallization, in which

Peer reviewed version of the manuscript published in final form at ACS Nano, 2019,
DOI:10.1021/acsnano.8b06492.

abundant Mg and PPi ions precipitated in the presence of amplified DNA (AmpDNA). The AmpDNA was obtained from the RCA reaction with the addition of pyrophosphatase (PPase) and subsequent ethanol precipitation. Deoxynucleoside triphosphate (dNTP), deoxynucleoside monophosphate (dNMP), phi29 DNA polymerase (φ29 DNAP), pyrophosphate (PPi, P_2O_7), phosphate (Pi), magnesium pyrophosphate (Mg_2PPi), magnesium hydrogen phosphate (MgHPi).

We first prepared AmpDNA by performing RCA with the addition of PPase and purification, as described above (see detailed experimental procedures in Materials and Methods). In a typical nucleic acid amplification process using a DNA polymerase, the precipitation of Mg_2PPi gives rise to inhibition of DNA synthesis by causing a gradual decrease in free Mg ions required for DNAP activity in the reaction solution over time.[21,22] Therefore, when adding PPase to the RCA reaction mixtures, the production of DNA slightly increased due to the reduced amount of PPi as compared to the RCA products without PPase (Figure S1). We then examined the structural nature of AmpDNA by UV-visible (UV-Vis) absorption and circular dichroism (CD) spectroscopy. For comparison, we used phage lambda DNA (λ DNA), which is about 48.5 kb in length. The AmpDNA showed a single characteristic band at 260 nm in a UV-Vis spectrum and a negative peak at 245 nm and a positive peak at 280 nm in a CD spectrum, which are consistent with spectra of double-stranded λ DNA (Figure S2a and S2b). Both DNA solutions have absorbance ratios of ca. 1.87 and ca. 1.85 at 260 nm/280 nm, suggesting that they are of suitable purity for the next fabrication step. In the agarose gel electrophoresis analysis, the AmpDNA appeared as a high-molecular-weight band (> 35 kb), indicating that the RCA products were successfully synthesized. To gain more insight into the structure, we visualized both DNAs prepared on mica by atomic force microscopy (AFM) imaging in tapping mode (Figure S2c and S2d). The AmpDNA showed high-order complex, supercoiled, and elongated DNA strands with an average height of 0.47 ± 0.03 nm. While the AmpDNA showed double-stranded DNA

Peer reviewed version of the manuscript published in final form at ACS Nano, 2019,
DOI:10.1021/acsnano.8b06492.

(dsDNA)-like features from the CD spectrum and AFM imaging similar to λ DNA, it is well accepted that the RCA process robustly produces very long and concatemeric single-stranded DNA (ssDNA) products, in which the amplified DNA is continuously displaced from the cyclic template DNA by a φ29 DNAP. These RCA products have been extensively exploited as functional ssDNA units capable of binding to single-stranded oligonucleotides or forming secondary structures such as DNA aptamers, DNAzymes, and G-quadruplexes.[23] To study the nature of AmpDNA as RCA products, we performed thorough analysis of AmpDNA with several exo- and endo-nucleases and SYBR dyes specific for ssDNA and/or dsDNA cleavage and staining (see more details of experimental procedures and analysis in Supporting Information, Figure S3 and Table S2). We believe that the prepared AmpDNA as single-stranded RCA products represent a mix of ssDNA and dsDNA, but most likely form a large amount of dsDNA-like conformation as a result of random folding of very long, flexible ssDNA.

We investigated the structure of a set of Mg_2PPi/DNA composites, where abundant PPi and Mg ions were precipitated in the presence of AmpDNA or λ DNA in aqueous solution for 20 h by scanning electron microscopy (SEM) imaging. Following the previous studies, various concentrations of PPi (0.5, 1, and 2 mM) were precipitated with a fixed amount of DNA (4 μg) in the same buffer used in the RCA reaction. Figure 1a-c show the influence of DNA molecules on the formation of the composites. First, Mg_2PPi without DNA formed a random assembly comprising 1−2 μm sized ellipsoidal nanoflakes in-plane. Some of these assembled into spherical or rod-like irregular aggregates with an increase in Mg_2PPi concentration. In contrast, the inclusion of DNA led to the formation of relatively small, fairly uniform spherical particles with multi-petal flower-like morphology similar to that of DNF. This also led to time-dependent crystallization with changes in size and morphology (Figure S5). We further analyzed a single

Peer reviewed version of the manuscript published in final form at ACS Nano, 2019,
DOI:10.1021/acsnano.8b06492.

ellipsoidal nanoflake by chemical mapping using a transmission electron microscope (TEM) operating in scanning TEM (STEM) mode combined with energy dispersive X-ray spectroscopy (EDS) (Figure 1d). The STEM-EDS elemental maps confirmed the presence of O, Mg, and P in the nanoflake consisting of Mg_2PPi (or $Mg_2P_2O_7$).

As schematically depicted in Figure 1e, the presence of DNA molecules seems to have a significant effect on the formation of primary crystals and their growth. It is likely that the nucleation and crystal growth of Mg_2PPi are retarded when the DNA molecules are present. This may be due to the electrostatic and van der Waals dispersion interactions between DNA and Mg^{2+} ions,[24] effectively increasing the nucleation energy of Mg_2PPi while also reducing the overall crystal growth rate, thus leading to much finer particles. This observation is in line with biomineralization processes finely regulated by naturally occurring organic macromolecules (*e.g.* complexes of nucleic acids, peptides, proteins, or lipids), which are believed to participate actively in the nucleation and growth processes.[25-27] The location of such organics can alter morphologies, structures, and orientations of the minerals *via* interactions with ionic precursors or mineral phases. Therefore, it is of great interest to understand how features such as size, morphology and crystal lattice can be affected by the DNA additives, acting as growth inhibitors and particle stabilizers during crystallization events.

Peer reviewed version of the manuscript published in final form at ACS Nano, 2019,
DOI:10.1021/acsnano.8b06492.

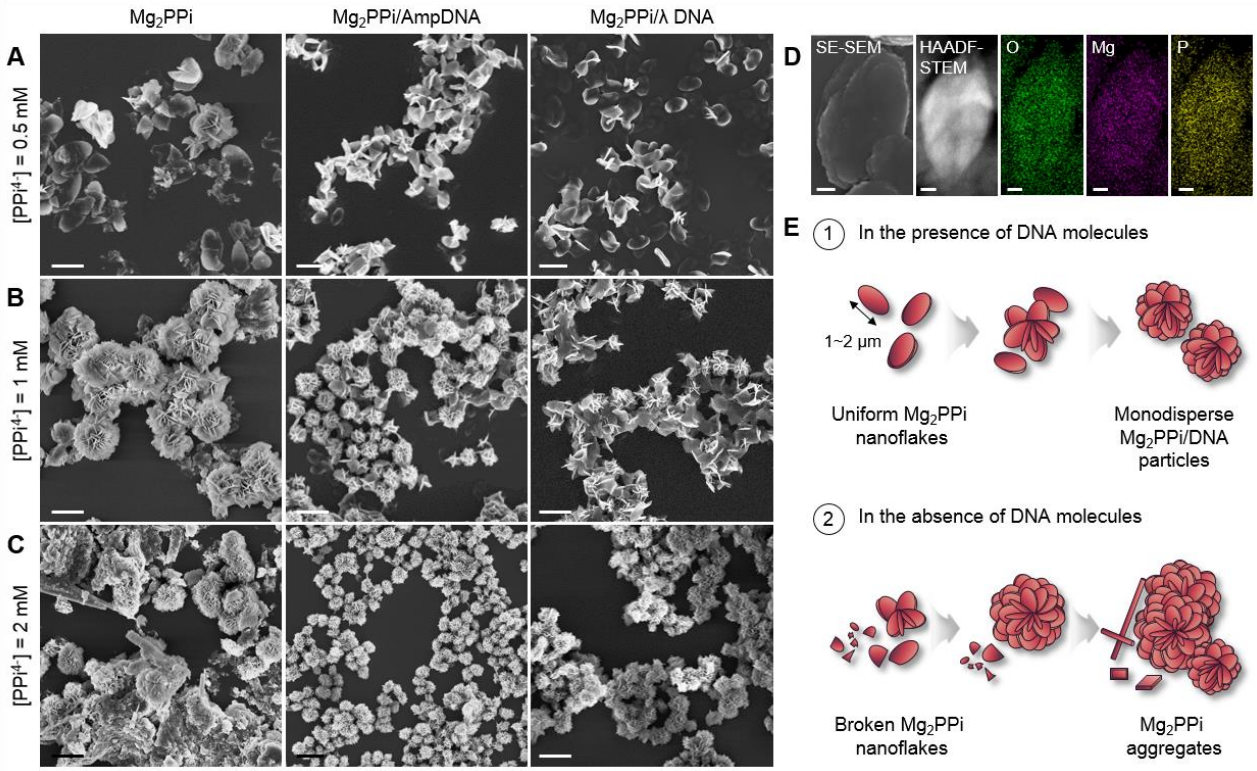

Figure 1. Inclusion of DNA as an organic additive in the formation of Mg_2PPi crystals. Representative SE-SEM images of the grown Mg_2PPi crystals after 20 h crystallization in the absence (left) and presence of AmpDNA (middle) and λ DNA (right) at a fixed concentration of DNA (26.7 μg mL^{-1}) and PPi ion concentrations of (A) 0.5 mM, (B) 1 mM and (C) 2 mM, where morphological changes are observed with increasing PPi ion concentrations. Scale bar, 2 μm. (D) SE-SEM and HAADF-STEM images of a nanoflake with ellipsoidal shape observed in the presence of 0.5 mM of Mg_2PPi. The EDS elemental maps confirmed the presence of oxygen (O), magnesium (Mg), and phosphorous (P) in the nanoflake. Scale bar, 200 nm. (E) Schematic illustration of the proposed role of DNA molecules in the regulation of the anisotropic growth of the Mg_2PPi nanoflakes.

We further performed a closer examination of single particles using both SEM and STEM. Using STEM, we can probe various aspects of a sample by collecting in parallel some of the multiple signals arising from interactions of the incident electron beam with a sample. Importantly, collecting the high angle annular dark field (HAADF) signal in the STEM produces

Peer reviewed version of the manuscript published in final form at ACS Nano, 2019,
DOI:10.1021/acsnano.8b06492.

an image where the image intensity (I) increases monotonically with specimen thickness and atomic number (Z), where $I \sim Z^{\alpha}$ and α is a parameter between 1.6 and 2.[28-30] The resulting HAADF-STEM image contrast is therefore often referred to as "Z-contrast": a higher or lower contrast indicates respectively heavier (higher atomic number) or lighter elements (lower atomic number) in the specimen, *i.e.* for a uniform specimen thickness. As shown in Figure S6, the Mg_2PPi particles possessed more hierarchical structures with increasing concentrations of PPi ions, in which densely packed backbones with bright image contrast indicate the materials with a high elemental density, assumed to be inorganic materials comprising O (Z = 8), Mg (Z = 12), and P (Z = 15).

Figure 2 shows high-resolution secondary electron SE-SEM and HAADF-STEM images of an individual particle of each formulation in conjunction with STEM-EDS analysis. Here we should note that we sought to find a single particle in Mg_2PPi with similar morphology to other composites for comparison, although they typically form aggregates with random size and morphology. As shown in Figure 2a, the Mg_2PPi particle exhibited a well-defined flower-like structure, consisting of several dozen nanoflakes with a smooth surface. The DNA-incorporated Mg_2PPi particles also exhibited similar morphologies, but with more interconnected networks of nanoflakes, presumably connected by long DNA strands, as indicated by red arrows in the magnified views (Figure 2b-d). This is in good agreement with the HAADF-STEM images in Figure 2e-h. Notably, the observed inorganic backbones of the Mg_2PPi/DNA composites were nearly all curved with very few straight lines compared to Mg_2PPi alone, implying that the adsorption of DNA led to anisotropic inhibition of the growth of the inorganic phases. EDS spectra were obtained from the entire region of an individual particle of each sample and revealed that C, N, O, Mg, and P are the main elements present in all Mg_2PPi/DNA composites

(Figure 2i). The obtained EDS spectra were quantitatively analyzed with the Inca software that uses calculated k-factors based on uniform composition and thickness of the specimen. Based on this quantitative analysis, the relative atomic ratios of C/Mg, N/Mg, and O/Mg in Mg_2PPi/AmpDNA, Mg_2PPi/λ DNA, and DNF were higher than those in Mg_2PPi. However, their P/Mg ratios remained nearly the same, indicative of the incorporation of DNA within the particles (Figure 2j). We further confirmed the incorporation of DNA by performing AFM-based indentation experiments, showing a slightly decreased Young's modulus of ca. 3.5 ± 0.6, 6.0 ± 0.8, and 6.2 ± 0.5 MPa for Mg_2PPi/AmpDNA, Mg_2PPi/λ DNA, and DNF compared to bare Mg_2PPi particles (ca. 7.8 ± 2.0 MPa); thus Mg_2PPi crystals became slightly less stiff when DNA strands were present (not statistically significant).

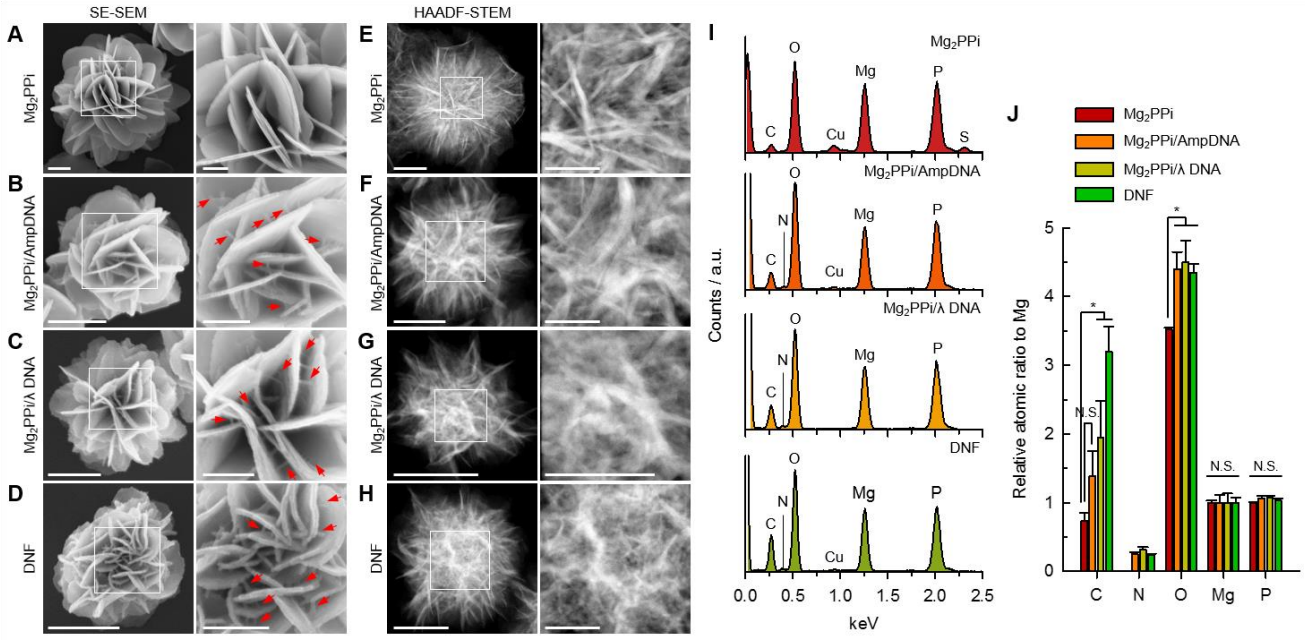

Figure 2. Structure and elemental composition of DNA-included Mg_2PPi composites. (A-D) Representative SE-SEM images of the Mg_2PPi crystals precipitated in (A) the absence and presence of (B) 26.7 μg mL^{-1} AmpDNA or (C) 26.7 μg mL^{-1} λ DNA with 2 mM Mg_2PPi. (D) In comparison, DNF was synthesized through one-step RCA reaction. High-magnification images show the presence of thin lines connecting the nanoflakes (indicated by red arrows) for

Peer reviewed version of the manuscript published in final form at ACS Nano, 2019,
DOI:10.1021/acsnano.8b06492.

Mg_2PPi/DNA and DNF, in contrast to the smooth nanoflake surfaces of Mg_2PPi. Scale bars, 500 nm (A-D, left) and 200 nm (A-D, right). (E-H) Representative HAADF-STEM images of each composite. The particle regions from which the higher magnification images (right) originated are indicated by boxes on the lower magnification HAADF-STEM images (left). Scale bars, 500 nm (E-H, left) and 200 nm (E-H, right). (I) EDS spectra recorded from entire individual particles. (J) Relative atomic ratios of each element, C, N, O, Mg, and P to Mg for each particle type. Data represent mean ± standard deviation (s.d.) of the EDS measurements determined over five particles. N.S. (not significant, $p > 0.05$) and $*p < 0.001$ based on one-way ANOVA and Tukey test's multiple comparison.

We also investigated the effect of AmpDNA concentration on composite formation. The particle size gradually decreased with increasing AmpDNA concentration, forming relatively small particles of 500−600 nm in size for an AmpDNA concentration of 53 μg mL^{-1} (Figure S7). Experimentally, the addition of a higher concentration of AmpDNA (> 53 μg mL^{-1}) slowed down the nucleation and inhibited the growth of the Mg_2PPi crystals such that any visible precipitates were not obtained after several washing steps. Therefore, these results suggest that the presence of DNA is of great importance for the spatial arrangement of inorganic Mg_2PPi backbones in the structure and affects the particle size and distribution through strong association with Mg_2PPi crystals. The length and structures of AmpDNA may also affect the crystallization of Mg_2PPi since a DNA molecule carries different numbers of charged phosphate groups depending on size or along the ssDNA or dsDNA chain,[31] which could influence the charge balance towards Mg^{2+}. A more comprehensive understanding of the effect of AmpDNA with varying sizes on Mg_2PPi formation could be achieved by tuning the RCA reaction time to produce smaller sized DNA products or by using other types of DNA, *e.g.* PCR products and short DNA oligonucleotides, smaller than AmpDNA in length. The structures of AmpDNA could be potentially modulated

using ssDNA-binding (SSB) proteins (*e.g.* T4 gene 32 protein, *E coli.* SSB), which are known to stabilize ssDNA regions in a cooperative way and to enhance specific activity and yield of DNAP in DNA amplification applications.[32] When introducing phage M13mp18 ssDNA as a control DNA, we observed that long ssDNA was effectively condensed with Mg_2PPi, leading to the formation of particles resembling Mg_2PPi/λ DNA composites (Figure S8).

In addition to DNA, we further crystallized Mg_2PPi in the presence of proteins with another organic additive, here RNase A (200 μg mL^{-1}), with or without AmpDNA (termed Mg_2PPi/AmpDNA-R or Mg_2PPi-R), and conducted identical analysis by STEM imaging and STEM-EDS. The protein additive yielded a similar particle morphology and configuration of the inorganic material as Mg_2PPi and similarly exhibited more curved morphology of the inorganic backbone with the inclusion of DNA and enzymes (Figure 3a-c). The EDS data indicate that all enzyme-containing composites have slightly increased O/Mg atomic ratios compared to the composites without the additional inclusion of enzymes (Figure 3d and 3e).

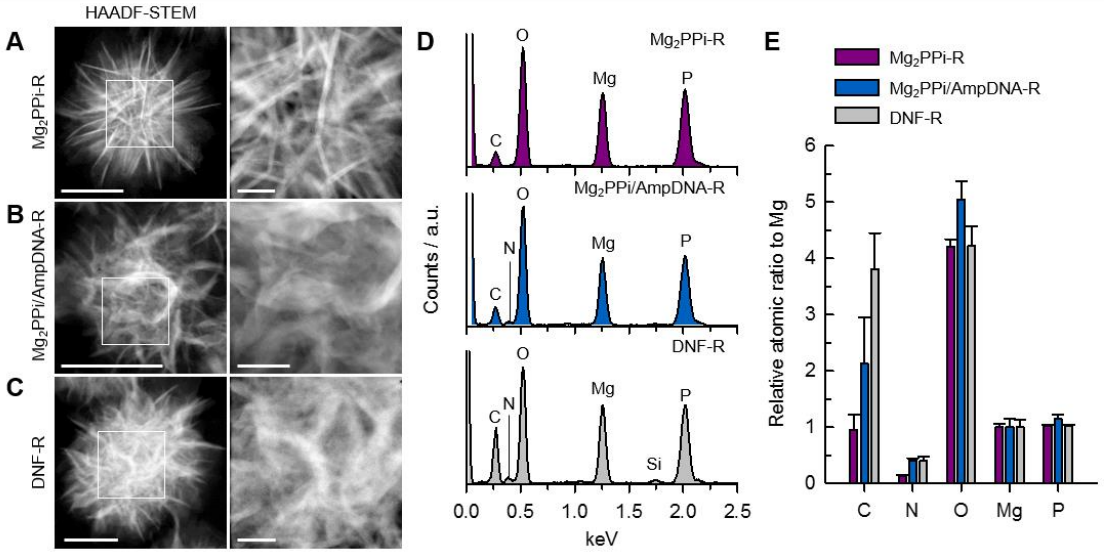

Figure 3. Structure and elemental composition of enzyme-included Mg_2PPi composites. (A-C) Representative HAADF-STEM images of the Mg_2PPi crystals precipitated in the presence of (A) RNase A and (B) RNase A and AmpDNA at 26.7 μg mL^{-1} DNA, 200 μg mL^{-1} RNase A and 2

mM Mg_2PPi. (C) In comparison, DNF-R was prepared through RCA reaction with the addition of RNase A. The particle regions from which the higher magnification images (right) originated are indicated by boxes on the lower magnification HAADF-STEM images (left). Scale bars, 500 nm (left) and 100 nm (right). (D) EDS spectra recorded from the whole area of the individual particle. (E) Relative atomic ratios of each element to Mg for each particle type. Data represent mean ± s.d. of the EDS measurements determined over five particles.

A direct observation of the spatial distribution of carbon and nitrogen provides a clear indication of organic materials such as DNA within the Mg_2PPi/DNA composites. The chemical bonding analysis of these two elements may offer some useful information on the molecular relationship between DNA and Mg_2PPi matrix at the nanoscale. Although we observed the presence of both elements in all DNA-incorporated composites from the EDS analysis, mapping the elemental distribution within the particles with EDS is hampered by the technique's relatively low sensitivity to lighter elements such as C, N, and O.[33] In contrast, electron energy loss spectroscopy (EELS) provides a higher sensitivity for lighter elements in combination with a much higher energy resolution, as compared to EDS.[34,35] The higher energy resolution allows not only for elemental mapping, but also for resolving spectral features in EELS ionization edges that can be attributed to specific chemical bonding states of the probed material down to atomic spatial resolution,[36,37] and even of single atom defects.[38] Therefore, to systematically study the localization of organics and their chemical bonding arrangements within the composites, we used EELS in a TEM (operating in STEM mode) on DNA, enzyme-embedded Mg_2PPi composites (Mg_2PPi/AmpDNA-R) and DNF-R.

For the EELS analysis, we prepared a site-specific lamellar sample with a thickness of 80−100 nm using the focused ion beam (FIB) lift-out technique (Figure S9).[39,40] For EELS acquisition, we cooled down the sample to cryo-temperature (-180 °C) inside the TEM using liquid nitrogen.

Peer reviewed version of the manuscript published in final form at ACS Nano, 2019,
DOI:10.1021/acsnano.8b06492.

Following this, we obtained the EEL spectral maps using raster scans with a 18−20 nm pixel size and de-noised them using the principal component analysis (PCA) to enhance weak signals in the spectrum (see detailed procedures in Materials and Methods). Figure 4 and S10 show the STEM and EELS characterization of the sliced sections of Mg_2PPi/AmpDNA-R and DNF-R prepared by FIB. Maps of C, N, and O for both composites were generated from the corresponding absorption *K*-edges of C, N, and O in the EEL spectrum, which suggests that all elements of interest are present over the selected areas of the particles (Figure 4b and 4g).

The study of C and N *K*-edges was of particular interest to identify differences in specific chemical compositions between the two composites. Therefore, we first analyzed the fine structure of the C *K*-edge in various selected regions from the edge to center of the Mg_2PPi/AmpDNA-R using Gaussian peak fitting. We assigned three peaks to three different atomic configurations: peak A at ~ 285 eV assigned to 1s-π* transitions in aromatic carbon bonds, peak B between 286 and 288 eV attributable to 1s-π* transitions in organic carbon bonds (*e.g.* carbonly carbon groups in aromatic rings, aromatic carbon bonds attached to amide groups, carbonyl and pyrimidine carbon bonds, *etc.*), possibly from nucleic acids and proteins, and peak C at ~290 eV mainly corresponding to 1s-π* transitions in carbonate (Figure 4c and 4d).[41-45] Specifically, the carbonate signal (peak C) was more pronounced in the center (EELS point 6 compared to point 1 in Figure 4a), while the organic carbon feature (peak B) was evenly preserved over the selected area of the particle. We observed the N *K*-edge at ~399 eV (peak D), most likely assigned to the 1s-π* transitions for nitrogen in an aromatic ring such as pyridine or amide group.[43-45] However, as the intensity of N *K*-edge was weak due to low signal-to-noise, we could not resolve the fine structure of the N *K*-edge.

Peer reviewed version of the manuscript published in final form at ACS Nano, 2019,
DOI:10.1021/acsnano.8b06492.

The *K*-edges of carbon and nitrogen in the DNF-R were relatively similar in their dominant functional groups: particularly in the C *K*-edge, aromatic carbon bonds at ~284 eV (peak A), organic carbon bonds between 286 and 288 eV (peak B), and carbonate at ~289 eV (peak C) (Figure 4h and 4i). We also obtained a reference spectrum from the platinum-covered region to evaluate if the observed peak features could be attributed to contamination during the sample preparation procedure (Figure S11). The C *K*-edge from the platinum-covered region showed a significant increase in the contribution of spectral features consistent with the ~285 eV 1s-π* and ~292 eV 1s-σ* peaks of amorphous and graphitic carbons,[46] rather than an increase in the relative contribution of peaks B and C. This confirmed that the B and C peaks are associated with organic and carbonate bonding inside the particle, rather than any superimposed carbon originating from the platinum deposition. Moreover, as indicated by the ratio maps of peaks B and C to the total C *K*-edge intensity, both composites showed a relatively higher content of organic carbon bonding (peak B) at the edge of the particles compared to the central region, implying that organic materials such as DNA and enzymes are more likely to be localized on the periphery of the particles (Figure 4e and 4j).

Peer reviewed version of the manuscript published in final form at ACS Nano, 2019,
DOI:10.1021/acsnano.8b06492.

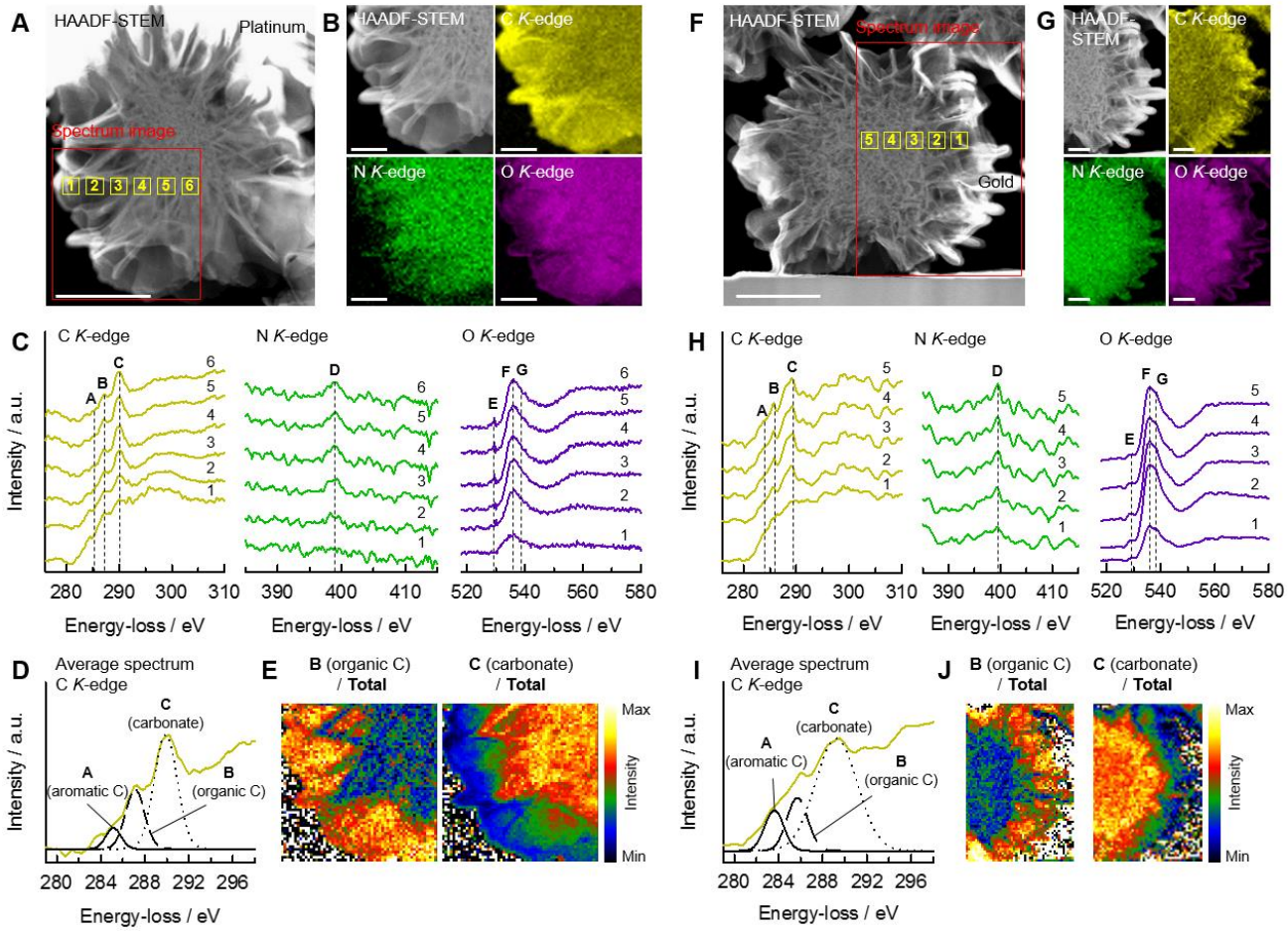

Figure 4. Spatially resolved STEM-EELS elemental analysis of (A-E) Mg_2PPi/AmpDNA-R and (F-J) DNF-R. (A, F) Representative HAADF-STEM images of the lamellar Mg_2PPi/AmpDNA-R and DNF-R specimens showing the highly porous interior. Scale bar, 500 nm. (B, G) HAADF images and EELS elemental maps (with an 18−20 nm pixel size) extracted from the area marked as "spectrum image" in (A) and (F), displaying the distribution of carbon (C K-edge), nitrogen (N K-edge), and oxygen (O K-edge). Scale bar, 200 nm. (C, H) Evolution of C K-, N K-, and O K-EELS spectra recorded over an area of 5×5 pixels or 4×4 pixels from the regions numbered 1-6, as marked in (A) and (F). (D, I) Average C K-edge EELS spectra fitted with Gaussian peaks. Peaks A (284−285 eV), B (286−287 eV), and C (289−290 eV) were assigned to aromatic carbon (aromatic C), organic carbon (organic C), and carbonate bonding, respectively. (E, J) The ratio maps of peak B, *i.e.* (organic C)/total intensity, and peak C, *i.e.* (carbonate)/total intensity, show the relative contribution of organic carbon and carbonate bonding within the particle. Ratio maps were generated by dividing intensity maps of peak B (organic C) and C (carbonate), resulting

Peer reviewed version of the manuscript published in final form at ACS Nano, 2019,
DOI:10.1021/acsnano.8b06492.

from Gaussian fitting of C K-edges in (D) and (I), by the respective total C K-edge intensities (integrated over 15 eV windows from the edge onsets).

The synthetic DNA-driven crystallization method provides a significant advantage for effective encapsulation of proteins of interest while not recruiting other enzymes (such as φ29 DNAP, DNA ligase and exonuclease) involved in the entire process of RCA-based DNF formulation. In this regard, we also speculated that the coincident participation of multiple proteins along with gradual elongation of DNA and production of Mg_2PPi during RCA might give rise to a relatively lower level of DNA inclusion than the Mg_2PPi/DNA composites prepared by the co-precipitation route. To assess whether DNA molecules can alter the ordering of the Mg_2PPi crystals by adhering to growing faces in different ways, the crystals grown in the absence or presence of DNA and/or enzymes were characterized by X-ray diffraction (XRD). The diffraction patterns of the composites clearly indicate that they exist in the phase of a hydrated magnesium pyrophosphate ($Mg_2P_2O_7{\cdot}3.5H_2O$).[47] There are no pronounced shifts in the peak positions measured for either Mg_2PPi/DNA composites or DNF regardless of enzyme inclusion, as compared with pure Mg_2PPi (Figure 5a). However, when DNA is introduced, they display peak broadening which spans the whole spectrum to some degree, ascribed to the inhomogeneous strain field caused by organic macromolecules as large entities within crystalline lattices, as reported in the literature.[48]

In order to ascertain how these DNA molecules are arranged in crystals, we further analyzed several Mg_2PPi composites formed by two approaches and showed their Raman spectra of the 600−1800 cm^{-1} region with most prominent bands and their assignment (Figure 5b and 5c, Table S4 and S5). Raman spectra provide clear evidence, in both types of composites (Mg_2PPi/AmpDNA and DNF), of the inclusion of DNA from the peaks in the 1100−1700 cm^{-1}

Peer reviewed version of the manuscript published in final form at ACS Nano, 2019,
DOI:10.1021/acsnano.8b06492.

region predominantly originating from in-plane C-C, C-N, C=N bond stretching or bending vibrations of nucleobases (Figure 5b).[49-51] In contrast, RNase entrapment into the composites displayed no appreciable peak changes compared to those without RNase A. When DNA is incorporated into Mg_2PPi, the characteristic DNA shoulder peak at ~784 cm^{-1} appears, attributed to the $\nu_s(OPO)$ vibration of DNA, whereas the peak at 762 cm^{-1} characteristic of the $\nu_s(POP)$ vibration of PPi appears in all spectra. The $\nu_s(PO_2)$ tentatively assigned to the vibration band of DNA, normally at 1090 cm^{-1}, is obscured by the strong $\nu_s(PO_2)$ vibration of PPi at 1063 cm^{-1} (Figure S13 and S14). The intensity ratio I_{784}/I_{762} or I_{784}/I_{1063}, which is indicative of the degree of covalency of the C-O-P-O-C bond of DNA phosphodiester backbones,[51] increased in DNA-incorporated composites compared to Mg_2PPi and showed a ca. 1.6−1.8-fold higher level for Mg_2PPi/AmpDNA than for DNF (Figure S15a). This result implies that the synthetic DNA-directed crystallization approach gave rise to a relatively higher level of the O-P-O environments of DNA in the composites, compared to those synthesized *via* a RCA-based one-pot process.

The phosphate (PO_2) region of the spectrum centered at 1063 cm^{-1} contains more information about the effect of DNA on the structure of these Mg_2PPi composites. The full width at half maximum (FWHM) of the phosphate band, which can be related to phase crystallinity,[52] further indicates that DNF exhibits a broader FWHM than Mg_2PPi or Mg_2PPi/AmpDNA (Figure S15b). This suggests a lower crystallinity of the Mg_2PPi phase caused by impeded packing and organization of the crystals through interactions with DNA and proteins. This is consistent with XRD profiles observed in DNF and DNF-R, which may also point to a decrease of the inter-chain strength of crystals experienced by the adsorption of DNA and reaction proteins during the RCA process. This protein association during RCA is further supported by three intense peaks strikingly appearing at 852, 919, and 1468 cm^{-1} in the Raman spectra of DNA and DNF-R,

Peer reviewed version of the manuscript published in final form at ACS Nano, 2019,
DOI:10.1021/acsnano.8b06492.

which can be considered as protein peaks.[53,54] More interestingly, these peaks nearly disappear when in aqueous solution (Figure 5c). Instead, an appearance of the broad peak around 832−835 cm^{-1}, which is characteristic of B-DNA conformation,[51] was detected in DNA-containing Mg_2PPi composites. As noted in Figure 5c and S13b, this peak originated from the ν_s(OPO) vibration of the polyphosphodiester bonds in DNA, and was not clearly detected in the air-dried samples due to the conformational transition of some of the DNA from physiological B-DNA to dehydrated A-form DNA.[55]

The UV absorption and CD spectra in aqueous solution similarly reveal the DNA-Mg_2PPi interaction. In Figure 5d and 5e, all composites except for Mg_2PPi showed a maximum in absorbance near 260 nm and a positive band at ~280 nm and a negative band at ~250 nm in CD signals, indicating that the secondary structure of DNA is maintained in the B-form even after condensation with Mg_2PPi.[56] However, we also note that Mg_2PPi/AmpDNA and Mg_2PPi/AmpDNA-R displayed a positive signal at 283 nm and a negative signal at 255 nm in the CD spectra, which are slightly red-shifted in comparison to the peaks observed for free AmpDNA, DNF, and DNF-R. This shift is therefore likely caused by alterations in helical arrangements and the asymmetric phosphate backbone of DNA, known to be induced by strong interactions with other molecules,[57] and here by Mg_2PPi, where we observed similar phenomena in their Raman spectra.

Finally, we investigated the catalytic activity of the RNase A embedded in Mg_2PPi/AmpDNA by monitoring the fluorescence of an RNA substrate labeled with a dye and quencher at the ends. The activity of free enzyme, Mg_2PPi-R, and DNF-R were also studied for comparison (Figure 5f and 5g). Interestingly, the enzyme encapsulation in Mg_2PPi/AmpDNA was almost as effective in overall activity as free enzyme, while the enzyme within Mg_2PPi or DNF exhibited ca. 2-fold

Peer reviewed version of the manuscript published in final form at ACS Nano, 2019,
DOI:10.1021/acsnano.8b06492.

lower activity at 20 min (Figure 5f). Based on the initial rate (the maximum slope, dΔF/dt) at various substrate concentrations (0.1−8 μM), we further calculated the K_m and V_{max} (kinetic parameters obtained from the Michaelis-Menten plot in Figure 5g) for each formulation. As reported in Table S3, the incorporated enzyme within the three composites gave negligible changes in the K_m, while only Mg_2PPi/AmpDNA-R showed a comparable V_{max} to free enzyme. This reveals that the DNA-mediated crystallization method leads to a more active catalyst than RCA-driven *in situ* synthesis, which accompanies other proteins and carryover reaction components. Moreover, Mg_2PPi/AmpDNA-R yielded a ca. 5-fold higher V_{max} than that in Mg_2PPi-R, consistent with the previous findings that highly ordered and hydrogen-bonded water environments of DNA structures in combination with high charge density are responsible for the enhancement of enzyme activity.[58] Although the RCA-based one-pot approach provides experimental simplicity for enzyme encapsulation, it contains various possibilities of thermal, chemical, and/or physical denaturation of the embedded enzyme due to the reaction conditions (temperature, reaction buffers, other reaction enzymes) required for typical nucleic acid amplification techniques. Therefore, the synthetic DNA-driven crystallization method offers distinct advantages, namely enabling encapsulation of a diverse range of enzymes, favorable reaction conditions (room temperature and neutral pH), and no non-selective association of other molecules.

Peer reviewed version of the manuscript published in final form at ACS Nano, 2019,
DOI:10.1021/acsnano.8b06492.

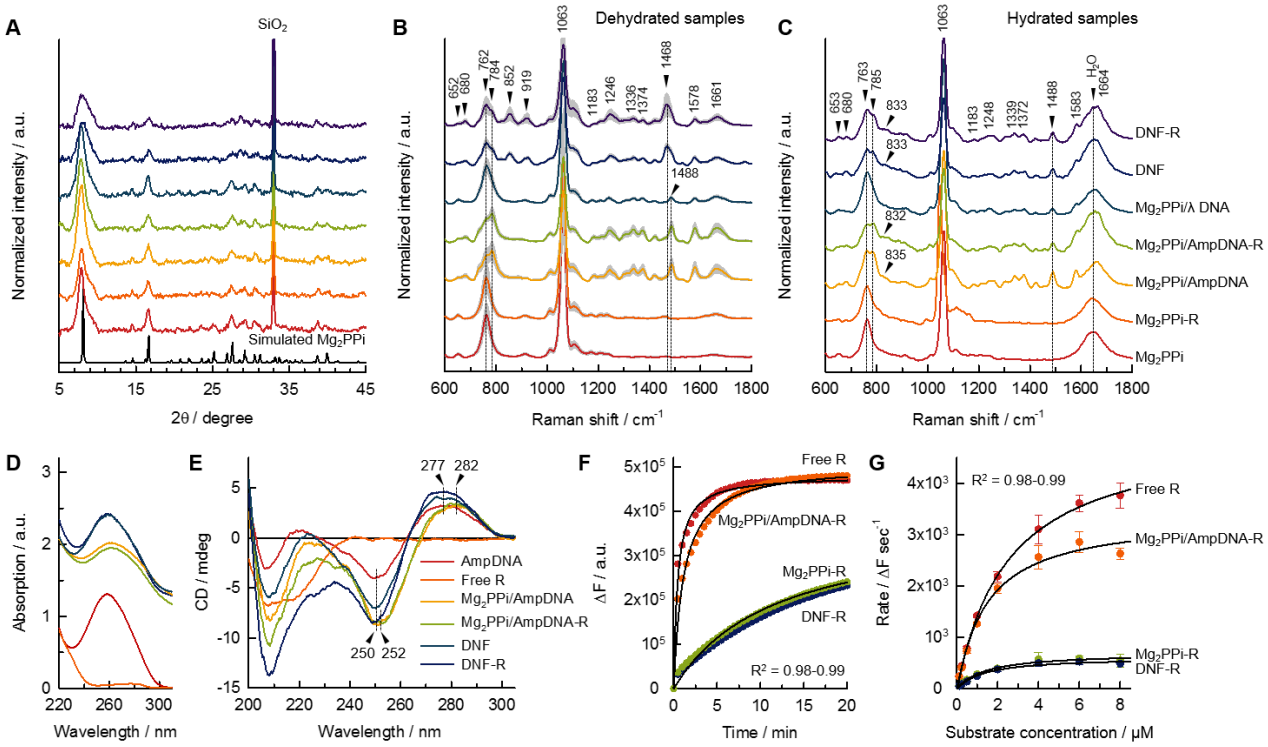

Figure 5. The effects of the inclusion of biomolecules on the growth of Mg_2PPi crystals. (A) Power XRD patterns and (B, C) Raman spectra of the Mg_2PPi composites grown in the absence/presence of DNA and/or RNase A (Mg_2PPi, Mg_2PPi-R, Mg_2PPi/AmpDNA, Mg_2PPi/AmpDNA-R, and Mg_2PPi/λ DNA) and DNF in the absence/presence of RNase A (DNF and DNF-R). A diffraction pattern of the simulated Mg_2PPi ($Mg_2P_2O_7{\cdot}3.5H_2O$) is also shown. The Raman spectra were obtained in (B) dehydrated and (C) hydrated conditions using a 532 nm laser. In (B), the spectra were obtained with a laser power of 13 mW and acquisition time of 5 sec and show the average spectra ± s.d. of five different points in the sample area. In (C), the spectra were collected with a laser power of 30 mW and acquisition time of 20 sec and show the spectra of one point in the sample area. All Raman spectra are normalized to the area under the curve. (D) UV absorption and (E) CD spectra of AmpDNA, free RNase A (free R), Mg_2PPi/AmpDNA, Mg_2PPi/AmpDNA-R, DNF, and DNF-R. (F) Fluorescence intensity ($\Delta F = F - F0$, where F and F0 are the emitted fluorescence of a substrate with and without treatment of RNase-containing samples at λ_{ex} = 490 nm and λ_{em} = 520 nm) as a function of time for four different catalytic systems. 4 μM of RNA substrate was used. (G) Reaction rate against various concentrations of the substrate (0.1−8 μM) for four catalytic systems. The concentration of

Peer reviewed version of the manuscript published in final form at ACS Nano, 2019,
DOI:10.1021/acsnano.8b06492.

RNase A in each sample was 0.5 ng mL^{-1}. Results represent mean ± s.d. for four independent experiments.

CONCLUSIONS

In this work, we demonstrate an approach for controlling the size, structure, and properties of Mg_2PPi crystals with well incorporated synthetic DNA molecules. In combination with our previous study on the fabrication of well-defined hybrid structures of Mg_2PPi/DNA composites through a one-pot enzymatic synthesis, we have shown that these composites can be formulated by precipitating abundant Mg and PPi ions with effectively isolated DNA, here AmpDNA, without association of non-selective adsorption of various proteins that can stem from the RCA reaction. As one of the key findings of our study, we report the influences of the inclusion of DNA as a macromolecular additive on the nucleation and growth kinetics, thereby controlling morphology and size of Mg_2PPi crystals. The DNA inclusion gave rise to the formation of relatively uniform, spherical Mg_2PPi/DNA particles with a more curved arrangement of inorganic phases, whereas Mg_2PPi without DNA led to a random assembly of crystals with irregular size and morphology. From the diverse spectroscopic characterizations, we also found that Mg_2PPi crystallization in the presence of DNA *via* the co-precipitation method led to the relatively higher crystallinity coupled with strong interaction with DNA compared to the RCA-based one-pot process. This denotes an alternative approach for RCA-driven protein encapsulation that is subjected to specific reaction conditions, such as temperature and reaction components, required for DNAP activity. Thus, our developed approach can be further extended to build protein-embedded DNA architectures using broad reaction conditions while taking advantage of the hydrated polymer-like DNA chains, demonstrating its potential as a biocatalytic

Peer reviewed version of the manuscript published in final form at ACS Nano, 2019,
DOI:10.1021/acsnano.8b06492.

enzyme complex. This approach exhibits great potential for even further biomedical applications, due to the ability to encapsulate a variety of biomolecules, such as proteins, DNA, and RNA.

MATERIALS AND METHODS

Preparation of AmpDNA. High-performance liquid chromatography-purified DNA oligonucleotides (Integrated DNA Technology, USA) were used without further purification (see Table S1 for details of DNA sequences). All enzymes and reagents used in rolling circle amplification (RCA) were obtained from New England Biolabs (USA). The amplified DNA (AmpDNA) was synthesized by carrying out the RCA reaction in the presence of pyrophosphatase (PPase) and subsequent purification with ethanol precipitation. To serve as a template for a typical RCA process, single-stranded DNA minicircles were first prepared by ligation of linear template DNA with T4 DNA ligase. Briefly, 5'-phosphorylated linear DNA (5 μM) was hybridized with a primer (10 μM) in ligase reaction buffer (50 mM Tris-HCl, 10 mM $MgCl_2$, 1 mM ATP, 10 mM DTT, pH 7.5) by heating at 95 °C for 5 min and slowly cooling to room temperature over 3 h. The nick in the hybridized DNA was chemically sealed by incubation with T4 DNA ligase (20 U μL^{-1}) in a reaction volume of 100 μL at 16 °C overnight. After heat inactivation of the enzyme at 65 °C for 10 min, to degrade excess primers the resulting mixture was further treated with exonuclease I (480 mU μL^{-1}) in reaction buffer (67 mM Glycine-KOH, 6.7 mM $MgCl_2$, 10 mM β-mercaptoethanol, pH 9.5) at 37 °C for 1.5 h (final volume of 250 μL). The enzyme was inactivated at 80 °C for 15 min. The resulting template DNA minicircle (2 μM) containing T4 DNA ligase (8 U μL^{-1}) and exonuclease I (480 mU μL^{-1}) was used for RCA reaction without further purification.

Peer reviewed version of the manuscript published in final form at ACS Nano, 2019,
DOI:10.1021/acsnano.8b06492.

For synthesis of AmpDNA, a typical RCA mixture in a final volume of 50 μL containing a DNA minicircle (0.6 μM), dNTPs (1 mM), phi29 DNA polymerase (φ29 DNAP, 1 U μL^{-1}), and PPase (2 mU μL^{-1}) was prepared in reaction buffer (50 mM Tris-HCl, 10 mM $MgCl_2$, 10 mM $(NH_4)_2SO_4$, 4 mM DTT, pH 7.5). The reaction was performed at 30 °C for 20 h and terminated by inactivation of the DNAP at 65 °C for 10 min. It is important to note that relatively large amounts of DNA ligase (120 U, 2.4 U μL^{-1}) and exonuclease I (7 U, 144 mU μL^{-1}) still remained along with 50 U of DNAP (1 U μL^{-1}) in 50 μL of RCA products. The RCA products were desalted and precipitated by ammonium acetate (2.5 M) and ethanol. The DNA pellet was dissolved in 10 mM Tris buffer (pH 8.0), fully unfolded by heating at 95 °C for 10 min, quenched on ice, and stored at -20 °C for further use.

Here the obtained AmpDNA is highly likely to contain both single-stranded (ssDNA) and double-stranded DNA (dsDNA). However, it is not practically straightforward to quantify the exact amount of each ssDNA and dsDNA present in AmpDNA as currently available DNA quantification methods detect both DNA strands to some extent. Based on the results in Figure S3, we assumed that the amount of ssDNA in AmpDNA could be negligible, and therefore used the PicoGreen dsDNA reagent (Thermo Fisher Scientific, UK) for quantification. The fluorescence-based PicoGreen measurement enables the measurement of the concentration of dsDNA with varying fragment sizes and molecular complexity with reliable sensitivity and efficiency as compared with the UV absorbance-based method.[59] The DNA concentration was then determined according to the manufacturer's protocols, based on the standard curve of serial dilutions of lambda DNA (λ DNA). The average repeating units in the resulting AmpDNA were estimated by following the previously reported methods (see detailed experimental procedures and analysis in Figure S4 and Table S3 in Supporting Information).[17,60] The pyrophosphate (PPi)

Peer reviewed version of the manuscript published in final form at ACS Nano, 2019,
DOI:10.1021/acsnano.8b06492.

concentration was assessed using the pyrophosphate assay kit (Abcam, UK) according to the manufacturer's protocols. The obtained values were inverted to PPi concentration using appropriate PPi standards.

Growth of Mg_2PPi in the Presence of AmpDNA and RNase A. To formulate Mg_2PPi/AmpDNA and Mg_2PPi/AmpDNA-R, magnesium pyrophosphate (Mg_2PPi or $Mg_2P_2O_7$) with varying concentrations (0.5−2 mM) was precipitated in the presence of AmpDNA (26.7 μg mL^{-1}) and/or RNase A (200 μg mL^{-1}). A stock solution of sodium pyrophosphate decahydrate ($Na_4P_2O_7{\cdot}10H_2O$, 20 mM, Sigma-Aldrich) dissolved in nuclease-free water was added to a solution of AmpDNA and/or RNase A in the RCA reaction buffer containing 10 mM $MgCl_2$. Precipitation was allowed to proceed at 30 °C. After 20 h, white precipitates were visible and washed with nuclease-free water by centrifugation at 5,000 g for 10 min. The obtained particles were redispersed in nuclease-free water and kept at 4 °C until use. For comparison, Mg_2PPi/λ DNA and Mg_2PPi/M13mp18 ssDNA were was also formed by precipitating Mg_2PPi in the presence of commercial lambda DNA (λ DNA, 26.7 and 40 μg mL^{-1}) and M13mp18 ssDNA (26.7 and 40 μg mL^{-1}) obtained from New England Biolabs.

Synthesis of DNF and DNF-R. DNA flowers (DNF) and RNase A-entrapped DNF (DNF-R) were prepared using the one-pot process of RCA, as described in our previous work.[8] For DNF-R, RNase A (600 μg mL^{-1}) was additionally added to the RCA reaction mixture in a final volume of 50 μL consisting of a DNA minicircle (0.6 μM), dNTPs (1 mM), and φ29 DNAP (1 U μL^{-1}) in the RCA reaction buffer. The RCA was carried out at 30 °C for 20 h, which is the same condition with the fabrication of Mg_2PPi/DNA composites, and further incubated at 65 °C for 10 min to inactivate DNAP. The DNF and DNF-R were then collected by centrifugal separation and washing of the RCA products with nuclease-free water and stored at 4 °C.

Peer reviewed version of the manuscript published in final form at ACS Nano, 2019,
DOI:10.1021/acsnano.8b06492.

SEM Imaging. For scanning electron microscopy (SEM) imaging, 2.5 μL of each sample solution in nuclease-free water was placed on a cleaned silicon wafer chip (about 5 mm × 5 mm) and air-dried at room temperature, followed by coating with 10 nm chromium in a Q150T S sputter coater (Quorum Technologies). SEM analysis was performed on a Leo Gemini 1525 FEG SEM equipped with a secondary electron in-lens detector operating at 5 kV.

Sample Preparation for TEM/STEM and EELS Analysis. The samples for TEM/STEM and EELS were prepared using a dual beam focused ion beam (FIB, FEI Helios NanoLab 600) (Figure S9). Briefly, a region of 14 μm × 2 μm with particles of interest was selected in SEM mode and coated with 1 μm electron deposited platinum at 5 kV. The region was further protected by 1 μm platinum deposited by ion beam operating at 93 pA, 30 kV. Two trenches of dimensions 18 μm × 4 μm × 4 μm (length × width × depth) were made on either side of platinum protected layer using 2.8 nA to 6.4 nA at 30 kV. The section was further thinned to 1 μm and then released from the base using 6.4 nA, 30 kV. The released sample was then lifted out using omniprobe manipulator and secured to a TEM lift-out 3 post copper grid (Agar Scientific) using platinum (1 μm thick). The sample section was further thinned down to approximately 80−100 nm thickness using currents in between 0.46 nA and 2.8 nA, 30 kV. Finally, the surface of the sample was cleaned and polished using ion beam operated at 10 pA, 2 kV to remove possible artifacts introduced by the ion milling.

STEM Imaging and EDS Analysis. The samples were prepared by placing 10 μL of the sample solution on 200-mesh carbon-coated Cu grids (Electron Microscopy Science, USA). Imaging in scanning transmission microscopy (STEM) mode and energy dispersive X-ray spectroscopy (EDS) analysis were performed on a JEOL JEM-2100F TEM operating at 200 kV, equipped with Gatan Orius SC 1000 (2 k × 4 k), Gatan high-angle annular dark-field (HAADF),

Peer reviewed version of the manuscript published in final form at ACS Nano, 2019,
DOI:10.1021/acsnano.8b06492.

Gatan annular bright field (BF), and EDS detectors (Oxford Instruments INCA EDS 80 mm X-Max detector system with STEM capability). The EDS spectra from the whole area of the individual particles were taken. Measurements over five particles per sample were used for elemental analysis. The obtained EDS spectra were quantitatively analyzed with a standardless approach and *k*-factors provided by the Inca software (Oxford Instruments).

EELS Acquisition and Analysis. For EELS acquisition, the FIB prepared sample was cooled down to cryo-temperature (-180 °C) using liquid nitrogen in the cryo-sample holder inside the TEM. The EELS was performed on a JEOL JEM-2100F TEM in STEM mode at 200 kV, equipped with STEM detectors (HAADF/BF), Gatan Quantum SE energy filter, and Gatan Orius SC 1000 (2 k × 4 k) camera. The spectral maps were collected with an energy resolution of ~ 1 eV and using a dispersion of 0.25 eV/channel. The exposure time was set to 0.5−1.0 sec, and spectra were acquired every 18−20 nm following 2D raster scans. The spatial drift was corrected in parallel, and high quality (HQ) dark correction was applied following the acquisition of EEL spectrum images.

For EELS analysis, principal component analysis (PCA) based de-noising was performed as implemented in the Multivariate Statistical Analysis (MSA) plugin for Gatan's DigitalMicrograph software 1.8 (commercially available from HREM Research Inc.). The 25 or 13 most significant components were included for reconstruction of the datasets used for the EELS analysis of Mg_2PPi/AmpDNA-R and DNF-R, respectively. The spectral maps were calibrated using the O *K*-edge at 536 eV. A power law background subtraction with a 10−20 eV window or wider was performed on all acquired edges. For carbon *K*- (C *K*-), nitrogen *K*- (N *K*-), and oxygen *K*- (O *K*-) edges, the fitting windows were set at 265−282 eV, 379−394 eV, 509−525 eV, respectively. To obtain elemental maps, the C, N, and O signals are integrated over the

Peer reviewed version of the manuscript published in final form at ACS Nano, 2019,
DOI:10.1021/acsnano.8b06492.

following energy windows: 284−291 eV (C *K*), 397−402 eV (N *K*), and 528−544 eV (O *K*). To quantify spectral peak properties, the C *K*-edge was fitted with Gaussian functions using the nonlinear least squares (NLLS) fitting tool available within DigitalMicrograph software 1.8 and subsequently plotted using SigmaPlot 12.0 (Systat Software Inc.). Ratio maps where created by dividing intensity maps of peaks B and C (resulting from the Gaussian fitting of the dataset, using peaks centered at 284−285 eV (A), 286−287 eV (B), and 289−290 eV (C)), by the total C *K*-edge intensity integrated over a 15 eV window from the edge onset (at 283 eV for Mg_2PPi/AmpDNA-R and at 281 eV for DNF-R). The peaks were assigned using the available XANES and EELS literature.[44,45,61-64]

XRD Measurements. For X-ray diffraction (XRD) measurements, the sample films on an oxygen plasma-treated silicon wafer chip (about 1 cm × 1 cm) were prepared by evaporation of aqueous sample solution in air. Diffraction patterns of the sample films were recorded on a PANalytical X'Pert Pro MPD (PANalytical, The Netherlands) using Cu K_α radiation (λ = 1.54 Å, 40 kV, 40 mA). The data were collected at angles from 5° to 60° with a step size of 0.03°, and a scan rate of 2° min^{-1}. The obtained results were analyzed using X'Pert HighScore Plus software.

Raman Spectroscopy Analysis. The sample solution dispersed in nuclease-free water was dropped onto a cleaned calcium fluoride Raman substrate (Crystran Ltd., UK) and air-dried overnight. For comparison, a droplet of the sample solution was placed on the substrate just before Raman measurements. Analysis was performed on a confocal Raman microspectroscopy system (alpha 300 R+, WITec GmbH, Germany) using a green laser (λ_{ex} = 532 nm) with maximum output of 75 mW and a ×20/0.4 NA microscope objective lens (EC Epiplan, Zeiss, Germany). The backscattered Raman signals were directed to the spectrometer using a 100 μm low OH silicon fiber, equipped with a thermoelectrically cooled, charge-coupled device camera

(Newton, Andor Technology Ltd., UK). Raman spectra were collected in the spectral range from 0 to 3,600 cm^{-1} under a laser power of ~13 mW with an acquisition time of 5 sec (for solid samples) and ~30 mW with an acquisition time of 20 sec (for liquid samples).

Raman data were processed using in-house written methods using MATLAB software (MathWorks Inc., USA). The data were firstly smoothed using the second-order Savitsky-Golay method with a window size of 9. For the baseline correction, a second-order polynomial was fitted to the smoothed spectrum in the range of 600−1,800 cm^{-1} and subtracted. All the spectra presented were subsequently normalized to the area under the curve, which removed any instrument effects and enabled comparisons between the samples by reducing the signal intensity variability. To determine the full width at half maximum (FWHM), the peak centered at 1063 cm^{-1} in the 1020−1110 cm^{-1} spectral region was fit to a Gaussian profile using OriginPro 9.1 software. The peaks were assigned with the literature data.[49-51,53-55]

UV Absorption and CD Measurements. The samples were redispersed in 10 mM Tris buffer (pH 8.0). The UV absorption and circular dichroism (CD) signals were recorded on a Perkin Elmer Lambda 25 UV/Vis spectrometer in a 1.0 cm quartz cuvette and JASCO J-715 spectrometer in a 0.1 cm quartz cuvette, respectively. The CD data were collected at room temperature with two scan accumulations at a scan rate of 50 nm min^{-1} with a 0.1 nm pitch and 4 sec integration time.

RNase Activity Test. The ribonucleotic activity of RNase A was evaluated using a synthetic RNA oligonucleotide, which has a fluorescein dye and quencher at both ends (RNase Alert substrate, Integrated DNA Technology). Before testing, the protein concentration of each sample was measured by Qubit protein reagent (Thermo Fisher Scientific), based on the standard curve using free RNase A with known concentrations (0, 200, and 400 ng μL^{-1}). Protein-containing

Peer reviewed version of the manuscript published in final form at ACS Nano, 2019,
DOI:10.1021/acsnano.8b06492.

sample solution (10 μL) was mixed with 190 μL of Qubit working solution prepared by diluting 200-fold the Qubit protein reagent in assay buffer according to the manufacturer's instructions. After incubation at room temperature for 15 min, the fluorescence was measured with the Qubit 2.0 fluorometer. The amount of encapsulated RNase A in DNF-R was calculated by subtracting the measured concentration in DNF as a blank sample (which possibly entraps other proteins such as DNAP, ligase, or exonuclease) from that in DNF-R. Given that there are no proteins associated during particle formation, the measured concentrations of Mg_2PPi-R and Mg_2PPi/AmpDNA-R were used without subtraction of a blank sample, here Mg_2PPi. RNase activity assays were performed at room temperature by adding 10 μL of the RNase Alert substrate with an increasing concentration (0.1−8 μM) to 90 μL of each sample with an enzyme concentration of 0.5 ng mL^{-1}. 50 mM Tris buffer (pH 8.0) was used as an assay buffer. The fluorescence intensity at an excitation of 490 nm and an emission of 520 nm was monitored for 30 min using the EnVision multilabel plate reader (Perkin Elmer, USA). The K_m and V_{max} were extracted from the Michaelis-Menten and Lineweaver-Burk plots (Figure 5g and S16), based on the following equation: $1/V = (K_m/V_{max}) \times [S] + 1/V_{max}$, where V is the initial catalytic rate, K_m is the Michaelis-Menten constant, V_{max} is the maximum catalytic rate, and [S] is the substrate concentration. The initial rate of the enzyme was obtained by measuring a change in fluorescence intensity of the sample and substrate over time, as shown in Figure 5f.

ASSOCIATED CONTENT

Supporting Information. The Supporting Information is available free of charge on the ACS Publication website.

Peer reviewed version of the manuscript published in final form at ACS Nano, 2019, DOI:10.1021/acsnano.8b06492.

Details of experiments (gel electrophoresis, AFM imaging and indentation, analysis of AmpDNA with nucleases and SYBR dyes, SIM imaging), additional notes, figures, and tables, including characterization of AmpDNA, HAADF-STEM images of a single Mg_2PPi particle, SE-SEM images and size distribution of various Mg_2PPi/DNA composites, time-dependent formation of Mg_2PPi/AmpDNA, the FIB lift-out technique procedures, HAADF-STEM images of the lamellar specimens prepared by the FIB, EELS reference spectrum from the platinum region, SIM imaging and Raman spectra analysis of various Mg_2PPi composites, and tables of nucleic acid sequences, nuclease properties, estimated average repeating units in AmpDNA, tentative Raman band assignment, and enzyme kinetics of various Mg_2PPi composites (PDF).

AUTHOR INFORMATION

Corresponding Author

*E-mail: m.stevens@imperial.ac.uk

ACKNOWLEDGMENTS

E.K. acknowledges support from Basic Science Research Program through the National Research Foundation of Korea (NRF) funded by the Ministry of Education (2015R1A6A3A03018919). A.G. acknowledges support from the European Union's Horizon 2020 Research and Innovation Programme through the Marie Skłodowska-Curie Individual Fellowship "RAISED" under grant agreement no. 660757. M.M.S. acknowledges support from the ERC Seventh Framework Programme Consolidator grant "Naturale CG" (616417), the Wellcome Trust Senior Investigator Award (098411/Z/12/Z), the EPSRC grant "Bio-functionalised nanomaterials for ultrasensitive biosensing" (EP/K020641/1) and i-sense EPSRC

IRC in Early Warning Sensing Systems for Infectious Diseases (EP/K031953/1). The authors would like to thank Dr. M. S. Bergholt for the critical reading of this manuscript and insightful comments and the Harvey Flower Electron Microscopy Suite at Imperial College London for support with SEM and TEM characterization. SIM imaging was performed in the Facility for Imaging by Light Microscopy (FILM) and is partly supported by the BBSRC (BB/L015129/1). The SuperSTEM Laboratory is the U.K. National Research Facility for Advanced Electron Microscopy, supported by the Engineering and Physical Sciences Research Council (EPSRC). Raw data are available at DOI: 10.5281/zenodo.2560145.

REFERENCES

1. Heuer, A. H.; Fink, D. J.; Laraia, V. J.; Arias, J. L.; Calvert, P. D.; Kendall, K.; Messing, G. L.; Blackwell, J.; Rieke, P. C.; Thompson, D. H.; Wheeler, A. P.; Veis, A.; Caplan, A. I. Innovative Materials Processing Strategies: A Biomimetic Approach. *Science* **1992**, *255*, 1098-1105.

2. Mann, S.; Archibald, D. D.; Didymus, J. M.; Douglas, T.; Heywood, B. R.; Meldrum, F. C.; Reeves, N. J. Crystallization at Inorganic-Organic Interfaces: Biominerals and Biomimetic Synthesis. *Science* **1993**, *261*, 1286-1292.

3. Song, R.-Q.; Colfen, H. Additive Controlled Crystallization. *CrystEngComm* **2011**, *13*, 1249-1276.

4. Lee, J. B.; Hong, J.; Bonner, D. K.; Poon, Z.; Hammond, P. T. Self-Assembled RNA Interference Microsponges for Efficient siRNA Delivery. *Nat. Mater.* **2012**, *11*, 316-322.

5. Zhu, G.; Hu, R.; Zhao, Z.; Chen, Z.; Zhang, X.; Tan, W. Noncanonical Self-Assembly of Multifunctional DNA Nanoflowers for Biomedical Applications. *J. Am. Chem. Soc.* **2013**, *135*, 16438-16445.

6. Hu, R.; Zhang, X.; Zhao, Z.; Zhu, G.; Chen, T.; Fu, T.; Tan, W. DNA Nanoflowers for Multiplexed Cellular Imaging and Traceable Targeted Drug Delivery. *Angew. Chem., Int. Ed.* **2014**, *53*, 5821-5826.

7. Shopsowitz, K. E.; Roh, Y. H.; Deng, Z. J.; Morton, S. W.; Hammond, P. T. RNAi-Microsponges Form Through Self-Assembly of the Organic and Inorganic Products of Transcription. *Small* **2014**, *10*, 1623-1633.

8. Kim, E.; Zwi-Dantsis, L.; Reznikov, N.; Hansel, C. S.; Agarwal, S.; Stevens, M. M. One-Pot Synthesis of Multiple Protein-Encapsulated DNA Flowers and Their Application in Intracellular Protein Delivery. *Adv. Mater.* **2017**, *29*, 1701086.

9. Sun, W.; Jiang, T.; Lu, Y.; Reiff, M.; Mo, R.; Gu, Z. Cocoon-Like Self-Degradable DNA Nanoclew for Anticancer Drug Delivery. *J. Am. Chem. Soc.* **2014**, *136*, 14722-14725.

10. Jang, M.; Kim, J. H.; Nam, H. Y.; Kwon, I. C.; Ahn, H. J. Design of a Platform Technology for Systemic Delivery of siRNA to Tumours Using Rolling Circle Transcription. *Nat. Commun.* **2015**, *6*, 7930.

11. Sun, W.; Ji, W.; Hall, J. M.; Hu, Q.; Wang, C.; Beisel, C. L.; Gu, Z. Self-Assembled DNA Nanoclews for the Efficient Delivery of CRISPR–Cas9 for Genome Editing. *Angew. Chem., Int. Ed.* **2015**, *54*, 12029-12033.

12. Wang, C.; Sun, W.; Wright, G.; Wang, A. Z.; Gu, Z. Inflammation-Triggered Cancer Immunotherapy by Programmed Delivery of CpG and Anti-PD1 Antibody. *Adv. Mater.* **2016**, *28*, 8912-8920.

13. Zhu, G.; Mei, L.; Vishwasrao, H. D.; Jacobson, O.; Wang, Z.; Liu, Y.; Yung, B. C.; Fu, X.; Jin, A.; Niu, G.; Wang, Q.; Zhang, F.; Shroff, H.; Chen, X. Intertwining DNA-RNA Nanocapsules Loaded with Tumor Neoantigens as Synergistic Nanovaccines for Cancer Immunotherapy. *Nat. Commun.* **2017**, *8*, 1482.

14. Merindol, R.; Loescher, S.; Samanta, A.; Walther, A. Pathway-Controlled Formation of Mesostructured All-DNA Colloids and Superstructures. *Nat. Nanotechnol.* **2018**, *13*, 730-738.

15. Ni, Q.; Zhang, F.; Zhang, Y.; Zhu, G.; Wang, Z.; Teng, Z.; Wang, C.; Yung, B. C.; Niu, G.; Lu, G.; Zhang, L.; Chen, X. *In Situ* shRNA Synthesis on DNA–Polylactide Nanoparticles to Treat Multidrug Resistant Breast Cancer. *Adv. Mater.* **2018**, *30*, 1705737.

16. Yuan, X.; Xiao, F.; Zhao, H.; Huang, Y.; Shao, C.; Weizmann, Y.; Tian, L. High-Yield Method To Fabricate and Functionalize DNA Nanoparticles from the Products of Rolling Circle Amplification. *ACS Appl. Bio Mater.* **2018**, *1*, 511-519.

17. Liu, M.; Zhang, Q.; Kannan, B.; Botton, G. A.; Yang, J.; Soleymani, L.; Brennan, J. D.; Li, Y. Self-Assembled Functional DNA Superstructures as High-Density and Versatile Recognition Elements for Printed Paper Sensors. *Angew. Chem. Int. Ed.* **2018**, *57*, 12440-12443.

18. Baker, Y. R.; Chen, J.; Brown, J.; El-Sagheer, A. H.; Wiseman, P.; Johnson, E.; Goddard, P.; Brown, T. Preparation and Characterization of Manganese, Cobalt and Zinc DNA Nanoflowers with Tuneable Morphology, DNA Content and Size. *Nucleic Acids Res.* **2018**, *46*, 7495-7505.

19. Gallagher-Jones, M.; Bessho, Y.; Kim, S.; Park, J.; Kim, S.; Nam, D.; Kim, C.; Kim, Y.; Noh, D. Y.; Miyashita, O.; Tama, F.; Joti, Y.; Kameshima, T.; Hatsui, T.; Tono, K.; Kohmura, Y.; Yabashi, M.; Hasnain, S. S.; Ishikawa, T.; Song, C. Macromolecular Structures Probed by Combining Single-Shot Free-Electron Laser Diffraction with Synchrotron Coherent X-Ray Imaging. *Nat. Commun.* **2014**, *5*, 3798.

20. Akama, S.; Yamamura, M.; Kigawa, T. A Multiphysics Model of *In Vitro* Transcription Coupling Enzymatic Reaction and Precipitation Formation. *Biophys. J.* **2012**, *102*, 221-230.

21. Dean, F. B.; Nelson, J. R.; Giesler, T. L.; Lasken, R. S. Rapid Amplification of Plasmid and Phage DNA Using Phi29 DNA Polymerase and Multiply-Primed Rolling Circle Amplification. *Genome Res.* **2001**, *11*, 1095-1099.

22. Mori, Y.; Nagamine, K.; Tomita, N.; Notomi, T. Detection of Loop-Mediated Isothermal Amplification Reaction by Turbidity Derived from Magnesium Pyrophosphate Formation. *Biochem. Biophys. Res. Commun.* **2001**, *289*, 150-154.

23. Ali, M. M.; Li, F.; Zhang, Z.; Zhang, K.; Kang, D.-K.; Ankrum, J. A.; Le, X. C.; Zhao, W. Rolling Circle Amplification: A Versatile Tool for Chemical Biology, Materials Science and Medicine. *Chem. Soc. Rev.* **2014**, *43*, 3324-3341.

24. Li, W.; Nordenskiöld, L.; Mu, Y. Sequence-Specific Mg2+–DNA Interactions: A Molecular Dynamics Simulation Study. *J. Phys. Chem. B* **2011**, *115*, 14713-14720.

25. Mann, S. Molecular Tectonics in Biomineralization and Biomimetic Materials Chemistry. *Nature* **1993**, *365*, 499-505.

26. Meldrum, F. C.; Cölfen, H. Controlling Mineral Morphologies and Structures in Biological and Synthetic Systems. *Chem. Rev.* **2008**, *108*, 4332-4432.

27. Sotiropoulou, S.; Sierra-Sastre, Y.; Mark, S. S.; Batt, C. A. Biotemplated Nanostructured Materials. *Chem. Mater.* **2008**, *20*, 821-834.

28. Midgley, P. A.; Weyland, M. 3D Electron Microscopy in the Physical Sciences: the Development of Z-Contrast and EFTEM Tomography. *Ultramicroscopy* **2003**, *96*, 413-431.

29. Thomas, J. M.; Midgley, P. A.; Yates, T. J. V.; Barnard, J. S.; Raja, R.; Arslan, I.; Weyland, M. The Chemical Application of High-Resolution Electron Tomography: Bright Field or Dark Field? *Angew. Chem. Int. Ed.* **2004**, *43*, 6745-6747.

30. Midgley, P. A.; Dunin-Borkowski, R. E. Electron Tomography and Holography in Materials Science. *Nat. Mater.* **2009**, *8*, 271-280.

31. Zhang, Y.; Zhou, H.; Ou-Yang, Z.-C. Stretching Single-Stranded DNA: Interplay of Electrostatic, Base-Pairing, and Base-Pair Stacking Interactions. *Biophys. J.* **2001**, *81*, 1133-1143.

32. Chase, J. W.; Williams, K. R. Single-Stranded DNA Binding Proteins Required for DNA Replication. *Annu. Rev. Biochem.* **1986**, *55*, 103-136.

33. Lugg, N. R.; Kothleitner, G.; Shibata, N.; Ikuhara, Y. On the Quantitativeness of EDS STEM. *Ultramicroscopy* **2015**, *151*, 150-159.

34. Egerton, R. F. Electron Energy-Loss Spectroscopy in the TEM. *Rep. Prog. Phys.* **2009**, *72*, 016502.

35. Kothleitner, G.; Grogger, W.; Dienstleder, M.; Hofer, F. Linking TEM Analytical Spectroscopies for an Assumptionless Compositional Analysis. *Microsc. Microanal.* **2014**, *20*, 678-686.

36. Muller, D. A. Structure and Bonding at the Atomic Scale by Scanning Transmission Electron Microscopy. *Nat. Mater.* **2009**, *8*, 263-270.

37. Kothleitner, G.; Neish, M. J.; Lugg, N. R.; Findlay, S. D.; Grogger, W.; Hofer, F.; Allen, L. J. Quantitative Elemental Mapping at Atomic Resolution Using X-Ray Spectroscopy. *Phys. Rev. Lett.* **2014**, *112*, 085501.

38. Ramasse, Q. M.; Seabourne, C. R.; Kepaptsoglou, D.-M.; Zan, R.; Bangert, U.; Scott, A. J. Probing the Bonding and Electronic Structure of Single Atom Dopants in Graphene with Electron Energy Loss Spectroscopy. *Nano Lett.* **2013**, *13*, 4989-4995.

39. Giannuzzi, L. A.; Stevie, F. A. A Review of Focused Ion Beam Milling Techniques for TEM Specimen Preparation. *Micron* **1999**, *30*, 197-204.

40. Wirth, R. Focused Ion Beam (FIB) Combined with SEM and TEM: Advanced Analytical Tools for Studies of Chemical Composition, Microstructure and Crystal Structure in Geomaterials on a Nanometre Scale. *Chem. Geol.* **2009**, *261*, 217-229.

41. Ade, H.; Zhang, X.; Cameron, S.; Costello, C.; Kirz, J.; Williams, S. Chemical Contrast in X-Ray Microscopy and Spatially Resolved XANES Spectroscopy of Organic Specimens. *Science* **1992**, *258*, 972-975.

42. Varlot, K.; Martin, J. M.; Gonbeau, D.; Quet, C. Chemical Bonding Analysis of Electron-Sensitive Polymers by EELS. *Polymer* **1999**, *40*, 5691-5697.

43. Vollmer, C.; Kepaptsoglou, D.; Leitner, J.; Busemann, H.; Spring, N. H.; Ramasse, Q. M.; Hoppe, P.; Nittler, L. R. Fluid-Induced Organic Synthesis in the Solar Nebula Recorded in Extraterrestrial Dust from Meteorites. *Proc. Natl. Acad. Sci. U. S. A.* **2014**, *111*, 15338-15343.

44. Nitiputri, K.; Ramasse, Q. M.; Autefage, H.; McGilvery, C. M.; Boonrungsiman, S.; Evans, N. D.; Stevens, M. M.; Porter, A. E. Nanoanalytical Electron Microscopy Reveals a Sequential Mineralization Process Involving Carbonate-Containing Amorphous Precursors. *ACS Nano* **2016**, *10*, 6826-6835.

45. Kłosowski, M. M.; Carzaniga, R.; Abellan, P.; Ramasse, Q.; McComb, D. W.; Porter, A. E.; Shefelbine, S. J. Electron Microscopy Reveals Structural and Chemical Changes at the Nanometer Scale in the Osteogenesis Imperfecta Murine Pathology. *ACS Biomater. Sci. Eng.* **2017**, *3*, 2788-2797.

46. Bernier, N.; Bocquet, F.; Allouche, A.; Saikaly, W.; Brosset, C.; Thibault, J.; Charaï, A. A Methodology to Optimize the Quantification of sp2 Carbon Fraction from K Edge EELS Spectra. *J. Electron Spectrosc. Relat. Phenom.* **2008**, *164*, 34-43.

47. Kongshaug, K. O.; Fjellvåg, H.; Lillerud, K. P. Synthesis and Crystal Structure of the Hydrated Magnesium Diphosphate Mg2P2O7·3.5H2O and Its High Temperature Variant Mg2P2O7·H2O. *Solid State Sci.* **2000**, *2*, 205-214.

48. Pokroy, B.; Fitch, A.; Zolotoyabko, E. The Microstructure of Biogenic Calcite: A View by High-Resolution Synchrotron Powder Diffraction. *Adv. Mater.* **2006**, *18*, 2363-2368.

49. Duguid, J.; Bloomfield, V. A.; Benevides, J.; Thomas Jr., G. J. Raman Spectroscopy of DNA-Metal Complexes. I. Interactions and Conformational Effects of the Divalent Cations: Mg, Ca, Sr, Ba, Mn, Co, Ni, Cu, Pd, and Cd. *Biophys. J.* **1993**, *65*, 1916-1928.

50. Duguid, J. G.; Bloomfield, V. A.; Benevides, J. M.; Thomas Jr., G. J. Raman Spectroscopy of DNA-Metal Complexes. II. The Thermal Denaturation of DNA in the Presence of Sr2+, Ba2+, Mg2+, Ca2+, Mn2+, Co2+, Ni2+, and Cd2+. *Biophys. J.* **1995**, *69*, 2623-2641.

51. Deng, H.; Bloomfield, V. A.; Benevides, J. M.; Thomas Jr., G. J. Dependence of the Raman Signature of Genomic B-DNA on Nucleotide Base Sequence. *Biopolymers* **1999**, *50*, 656-666.

52. Pemberton, J. E.; Latifzadeh, L.; Fletcher, J. P.; Risbud, S. H. Raman Spectroscopy of Calcium Phosphate Glasses with Varying Calcium Oxide Modifier Concentrations. *Chem. Mater.* **1991**, *3*, 195-200.

53. Gelder, J. D.; Gussem, K. D.; Vandenabeele, P.; Moens, L. Reference Database of Raman Spectra of Biological Molecules. *J. Raman Spectrosc.* **2007**, *38*, 1133-1147.

54. Zhu, G.; Zhu, X.; Fan, Q.; Wan, X. Raman Spectra of Amino Acids and Their Aqueous Solutions. *Spectrochim. Acta, Part A* **2011**, *78*, 1187-1195.

55. Japaridze, A.; Vobornik, D.; Lipiec, E.; Cerreta, A.; Szczerbinski, J.; Zenobi, R.; Dietler, G. Toward an Effective Control of DNA's Submolecular Conformation on a Surface. *Macromolecules* **2016**, *49*, 643-652.

56. Kypr, J.; Kejnovská, I.; Renčiuk, D.; Vorlíčková, M. Circular Dichroism and Conformational Polymorphism of DNA. *Nucleic Acids Res.* **2009**, *37*, 1713-1725.

57. Gray, D. M.; Ratliff, R. L.; Vaughan, M. R. [19] Circular Dichroism Spectroscopy of DNA. *Methods Enzymol.*, **1992**, *211*, 389-406.

58. Zhao, Z.; Fu, J.; Dhakal, S.; Johnson-Buck, A.; Liu, M.; Zhang, T.; Woodbury, N. W.; Liu, Y.; Walter, N. G.; Yan, H. Nanocaged Enzymes with Enhanced Catalytic Activity and Increased Stability Against Protease Digestion. *Nat. Commun.* **2016**, *7*, 10619.

59. Ahn, S. J.; Costa, J.; Emanuel, J. R. PicoGreen Quantitation of DNA: Effective Evaluation of Samples Pre- or Post-PCR. *Nucleic Acids Res.* **1996**, *24*, 2623-2625.

60. Liu, M.; Hui, C. Y.; Zhang, Q.; Gu, J.; Kannan, B.; Jahanshahi-Anbuhi, S.; Filipe, C. D. M.; Brennan, J. D.; Li, Y. Target-Induced and Equipment-Free DNA Amplification with a Simple Paper Device. *Angew. Chem. Int. Ed.* **2016**, *55*, 2709-2713.

61. Leinweber, P.; Kruse, J.; Walley, F. L.; Gillespie, A.; Eckhardt, K.-U.; Blyth, R. I. R.; Regier, T. Nitrogen K-edge XANES - An Overview of Reference Compounds Used to Identify `Unknown' Organic Nitrogen in Environmental Samples. *J. Synchrotron Radiat.* **2007**, *14*, 500-511.

62. Cody, G. D.; Ade, H.; Alexander, C. M. O'D.; Araki, T.; Butterworth, A.; Fleckenstein, H.; Flynn, G.; Gilles, M. K.; Jacobsen, C.; Kilcoyne, A. L. D.; Messenger, K.; Stanford, S. A.; Tyliszczak, T.; Westphal, A. J.; Wirick, S.; Yabuta, H. Quantitative Organic and Light-Element

Analysis of Comet 81P/Wild 2 Particles Using C-, N-, and O-μ-XANES. *Meteorit. Planet. Sci.* **2008**, *43*, 353-365.

63. Lehmann, J.; Solomon, D.; Brandes, J.; Fleckenstein, H.; Jacobsen, C.; Thieme, J. Synchrotron-Based Near-Edge X-Ray Spectroscopy of Natural Organic Matter in Soils and Sediments. In *Biophysico-Chemical Processes Involving Natural Nonliving Organic Matter in Environmental Systems*; Senesi, N., Xing, B., Huang, P. M., Eds.; John Wiley & Sons: Hoboken, NJ, 2009; pp 729-781.

64. Kłosowski, M. M.; Friederichs, R. J.; Nichol, R.; Antolin, N.; Carzaniga, R.; Windl, W.; Best, S. M.; Shefelbine, S. J.; McComb, D. W.; Porter, A. E. Probing Carbonate in Bone Forming Minerals on the Nanometre Scale. *Acta Biomater.* **2015**, *20*, 129-139.

Peer reviewed version of the manuscript published in final form at ACS Nano, 2019, DOI:10.1021/acsnano.8b06492.

TABLE OF CONTENTS (TOC) GRAPHIC

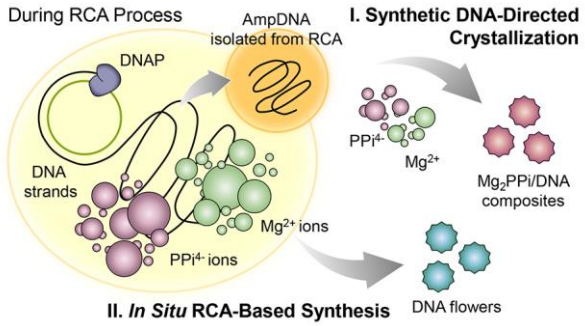

Peer reviewed version of the manuscript published in final form at ACS Nano, 2019, DOI:10.1021/acsnano.8b06492.

Supporting Information for

Bio-Inspired Fabrication of DNA-Inorganic Hybrid Composites Using Synthetic DNA

Eunjung Kim,[1] Shweta Agarwal,[1] Nayoung Kim,[1] Fredrik Sydow Hage,[2] Vincent Leonardo,[1] Amy Gelmi,[1] and Molly M. Stevens[1]*

[1]Department of Materials, Department of Bioengineering and Institute for Biomedical Engineering, Imperial College London, London, SW7 2AZ, United Kingdom

[2]SuperSTEM Laboratory, SciTech Daresbury Campus, Daresbury WA4 4AD, United Kingdom

Correspondence to:

*Email: m.stevens@imperial.ac.uk

Peer reviewed version of the manuscript published in final form at ACS Nano, 2019,
DOI:10.1021/acsnano.8b06492.

EXPERIMENTAL SECTION

Agarose and Polyacrylamide Gel Electrophoresis. The DNA samples were analyzed by 0.8% megabase agarose gel (Bio-Rad, USA) electrophoresis in 1× Tris/borate/EDTA (TBE) buffer. The gel was run at 50 V for 10 min and 100 V for 30 min, stained with SYBR Gold stain (Thermo Fisher Scientific) for 30 min at room temperature, and visualized with the BioSpectrum Imaging System (Ultra-Violet Products, UK). 2.5 kb DNA marker (Bio-Rad) and 1.0 kbp DNA marker (Thermo Fisher Scientific) were used as the reference standard. The gel images were processed with ImageJ software.

For native polyacrylamide gel electrophoresis, the prepared samples were run on a 10% polyacrylamide gel in 1× TBE buffer at 50 V for 10 min and 100 V for 60 min. For denaturing polyacrylamide gel electrophoresis, the samples were resolved on a 10% polyacrylamide gel containing 7 M urea in 1× TBE buffer at 80 V for 10 min and 120 V for 60 min. The urea-polyacrylamide gels were warmed by pre-running at 200 V for 1 h prior to loading and washed with 1× TBE buffer to remove excess urea. The samples were loaded after denaturation at 90 °C for 5 min in TBE-urea sample loading buffer. The gels were stained with SYBR Gold for 30 min and imaged with the BioSpectrum Imaging System. 10 bp DNA marker (Thermo Fisher Scientific) was used as the reference standard, and the obtained images were processed with ImageJ software.

AFM Imaging and Indentation Study. For sample preparation, the AmpDNA or λ DNA (1 μg mL^{-1}) was diluted in 10 mM HEPES buffer (pH 7.5) containing 5 mM nickel chloride, deposited onto a freshly cleaved mica sheet, and left to stand at room temperature for 10 min. The mica sheet was then rinsed with nuclease-free water several times to remove salts and unbound DNA

and dried with compressed air. Atomic force microscopy (AFM) imaging was conducted on an AFM 5500 microscope (Agilent Technologies, USA) in tapping mode in air. A HQ:NSC15/Al BS tip (MikroMasch, Germany) was used for the topography imaging. The images were processed with Gwyddion software.

To determine the Young's modulus of Mg_2PPi/DNA composites (Mg_2PPi, Mg_2PPi/AmpDNA, Mg_2PPi/λ DNA, and DNF), indentation experiments were conducted on an AFM 5500 microscope using the HQ:NSC15/Al BS cantilever with a calibrated spring constant of 5 N m^{-1}. Five particles per sample were indented with between one to five measurements per particle. The obtained force-distance curves were fitted using the free software AtomicJ.[1] The Young's modulus was calculated using the Hertz model assuming spherical indentation. The model was limited to an indentation depth less than 10% of the particle height in order to avoid substrate stiffness influence. Data are presented as mean Young's modulus ± standard error.

Analysis of the Nature of AmpDNA as RCA Products. To probe the nature of RCA products, comprehensive analysis of AmpDNA was performed using several enzymes and SYBR dyes specific for single-stranded (ssDNA) and/or double-stranded DNA (dsDNA) cleavage and staining. For enzyme digestion, two purified RCA products were prepared by performing RCA reaction at 30 °C for 20 h in the absence and presence of PPase (2 mU μL^{-1}), indicative of DNA strands present in DNF particles and AmpDNA strands (referred to as AmpDNA(-PPase) and AmpDNA(+PPase), respectively). For efficient isolation of DNA, Mg_2PPi precipitates in RCA products were dissolved by adding 20 mM EDTA solution at a 1:1 volume ratio and purified by ethanol precipitation. After purification, the resulting DNA was thermally fragmented by heating at 95 °C for 15 min to reduce the viscosity of highly concentrated intact AmpDNA, facilitating

easy control of DNA over the reaction with enzymes. The AmpDNA(-PPase) and AmpDNA(+PPase) were digested with four nucleases, including exonuclease I (Exo I), exonuclease III (Exo III), and exonuclease VII (Exo VII) obtained from New England Biolabs, and duplex-specific nuclease (DSN, Evrogen) at the optimized conditions. As a control, phage λ DNA, M13mp18 ssDNA (New England Biolabs), and synthetic 50 nt ssDNA oligonucleotide (Integrated DNA Technology, see the sequences in Table S1) were also tested. All DNA samples (45 μg mL^{-1}, 15 μL) were incubated in a reaction volume of 20 μL containing enzymes (20 U of Exo I, 100 U of Exo III, 10 U of Exo VII, and 0.25 U of DSN) at 37 °C (with Exo I, III, and VII) or 60 °C (with DSN) for 2 h. The reaction buffers provided from suppliers were used without modification. The digested products were resolved by 0.8% megabase agarose gel and 10% native polyacrylamide gel electrophoresis in 1× TBE buffer with post-staining using SYBR Gold stain.

The serial 2-fold dilutions of the purified AmpDNA(-PPase) and AmpDNA(+PPase) (initial concentration: 1 μg mL^{-1}) were further stained with 2× SYBR Green I, SYBR Green II, and SYBR Gold (Thermo Fisher Scientific) in parallel in TE buffer (10 mM Tris-HCl, 1 mM EDTA, pH 8.0). The mixtures were then incubated in a 96-well plate at room temperature for 15 min. The same concentrations of λ DNA and M13mp18 ssDNA were used as a control. The fluorescence intensity of SYBR Green I and SYBR Green II was recorded at an excitation of 497 nm and an emission of 520 nm using the EnVision multilabel plate reader. The fluorescence intensity of SYBR Gold was recorded at an excitation of 495 nm and an emission of 537 nm.

EcoRV Restriction Enzyme Treatments. In this experiment, different template DNA minicircles were used by replacing six base sequences of linear template with the restriction site

Peer reviewed version of the manuscript published in final form at ACS Nano, 2019,
DOI:10.1021/acsnano.8b06492.

GATATC recognized by EcoRV restriction endonuclease (New England Biolabs) (See Table S1 for details of nucleic acid sequences). To obtain AmpDNA, the RCA was performed with newly synthesized template DNA minicircles in the absence or presence of PPase in a final volume of 50 μL, and the RCA products were subsequently purified with ethanol and salt precipitation as described in Materials and Methods. The isolated AmpDNA was eluted in 100 μL of 10 mM Tris buffer (pH 8.0), and DNA concentration and purity were determined by PicoGreen assay and NanoDrop. The average repeating units in AmpDNA were estimated by following the procedures reported by Y. Li *et al*.[2,3] In detail, prior to digestion the AmpDNA (0.5 μL, 25 ng μL^{-1}) was hybridized with primers (1 μL, 100 μM) by heating at 90 °C for 5 min and slowly cooling to room temperature over 3 h. The resulting AmpDNA (0.6 ng μL^{-1}) was digested by EcoRV (5 U μL^{-1}) in 20 μL of CutSmart buffer (New England Biolabs) at 37 °C for 2 h. 2 μL of digestion products was then mixed with 1 μL of 50 nt DNA oligonucleotide (100 μM) as a loading control and 3 μL of 2× TBE-urea loading buffer, and analyzed by 10% denaturing urea-polyacrylamide gel electrophoresis.

SIM Imaging. For super-resolution structured illumination microscopy (SIM) imaging, a protein was chemically labeled with a primary amine-reactive fluorescent dye. Briefly, RNase A (2.5 mg mL^{-1}) was reacted with 5/6-carboxyfluorescein succinimidyl ester (fluorescein-NHS) at a 1:15 molar ratio in 50 mM borate buffer (pH 9.0) at room temperature for 4 h. Excess dyes were removed from the dye-labeled RNase A using a centrifugal filter device (MWCO 10 kDa) and redispersed in 50 mM Tris buffer (pH 8.0). The protein concentration was determined using a NanoDrop 2000c spectrometer (Thermo Fisher Scientific). The AmpDNA was enzymatically labeled with a dye through direct incorporation of Cyanine 3-deoxyuridine triphosphate (Cy3-

Peer reviewed version of the manuscript published in final form at ACS Nano, 2019,
DOI:10.1021/acsnano.8b06492.

dUTP) to the growing DNA strands during RCA reaction. Fluorescent AmpDNA was obtained by performing RCA in the presence of Cy3-dUTP (0.2 mM) and PPase (2 mU μL^{-1}) at 30 °C for 20 h, followed by purification with ethanol precipitation. The Mg_2PPi-R and Mg_2PPi/AmpDNA with fluorescently modified AmpDNA (26.7 μg mL^{-1}) and RNase A (200 μg mL^{-1}) were prepared using the co-precipitation method. The DNF and DNF-R were also fabricated by adding fluorescent RNase A (600 μg mL^{-1}) and Cy3-dUTP (0.2 mM) to the RCA reaction solution. The growth of those particles and purification by centrifugation were carried out in the same procedures as described above. 10 μL of the particles in nuclease-free water was briefly mixed into 190 μL of VectaShield mounting media (Vector Laboratories) and was pipetted onto an APTES-treated ibidi 8-well glass bottom μ-slide. The particles were left overnight to allow them to settle to the base of the slide. SIM imaging was then performed with the Zeiss Elyra PS1 system (Carl Zeiss, Germany).

Peer reviewed version of the manuscript published in final form at ACS Nano, 2019, DOI:10.1021/acsnano.8b06492.

Table S1. Nucleic acid sequences used in this study.

Name	Sequence (5' – 3')
Linear template DNA	Phosphorylation-AAT ATT ATT CCA GCT GGC GCT CGA GCT CGA GCC AGG TTG TAT CGT GAG ACT GCA CCT TGA ACG CTT ATT ATG ATT
Linear template DNA for EcoRV digestion	Phosphorylation -AAT ATT ATT CCA GCT GGC GCT CGA G***GA TAT C***CC AGG TTG TAT CGT GAG ACT GCA CCT TGA ACG CTT ATT ATG ATT
Primer for RCA	AAT AAT ATT AAT CAT AAT A
Primer for EcoRV digestion	GCT CGA G***GA TAT C***CC AGG TT
DNA as a loading control	ATT CCA GCT AAA CTC CCT GTA TCA AGC GTT TTC GGC AAA CCT GCT TCA TC

Letters in bold indicate the recognition site for EcoRV enzyme. Underlined sequences 'CTCGAG' in linear template DNA were replaced with the sequences 'GATATC' for EcoRV digestion.

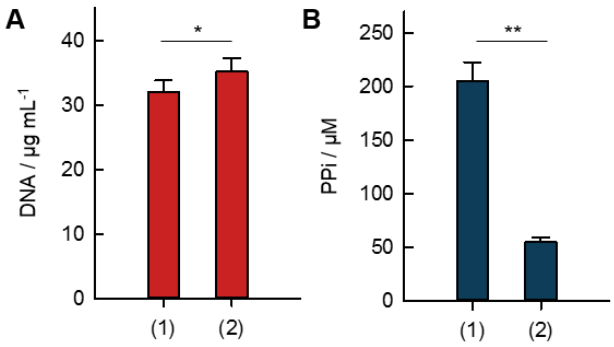

Figure S1. Quantification of (A) DNA and (B) PPi concentrations of AmpDNA isolated from the RCA reaction in the (1) absence and (2) presence of PPase. Data represent mean ± s.d. for N = 5. *$p < 0.05$ and **$p < 0.001$ determined by two-tailed *t*-test.

Peer reviewed version of the manuscript published in final form at ACS Nano, 2019,
DOI:10.1021/acsnano.8b06492.

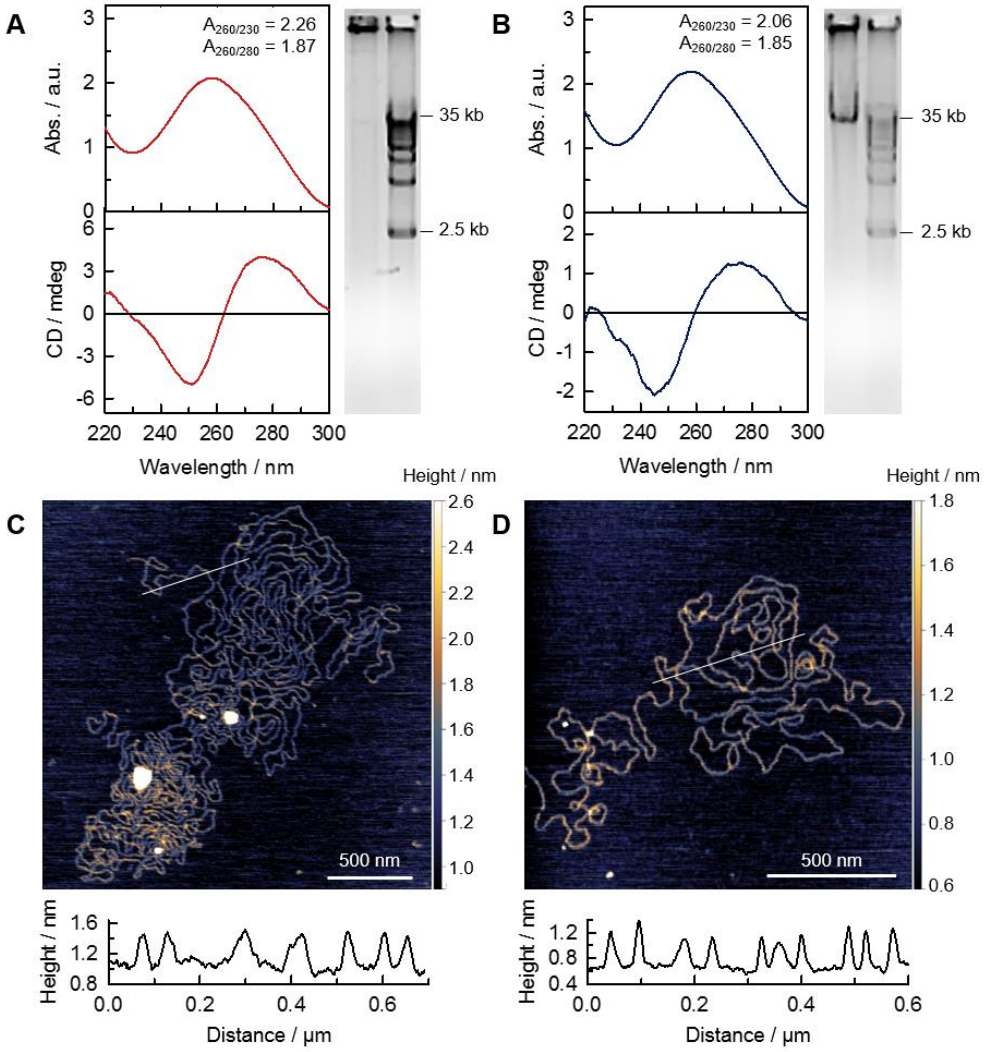

Figure S2. Characterization of AmpDNA and comparison with λ DNA. UV absorption and CD spectra of (A) AmpDNA and (B) λ DNA. Both DNA were resolved on a 0.8% megabase agarose gel. 2.5 kb DNA marker was used as a reference. Representative AFM images of (C) AmpDNA and (D) λ DNA with corresponding height profiles of the DNA products marked in (C) and (D). The measured height was 0.47 ± 0.03 nm and 0.54 ± 0.11 nm for AmpDNA and λ DNA, respectively.

Peer reviewed version of the manuscript published in final form at ACS Nano, 2019,
DOI:10.1021/acsnano.8b06492.

Note 1. Analysis of the Nature of AmpDNA. In this experiment, we digested AmpDNA(-PPase) and AmpDNA(+PPase) with four nucleases at the optimized conditions (*i.e.* at 37 °C for 2 h with Exo I, Exo III, and Exo VII, and at 60 °C for 2 h with DSN) and resolved by 0.8% agarose gel electrophoresis (Figure S3a and S3b). The results demonstrated that the multimeric DNA products obtained from both preparations showed a smear high molecular weight band with no defined lengths. This band was significantly eliminated by treatments with Exo III and DSN, but not affected by the addition of Exo I and Exo VII. For comparison, we further tested various forms of DNA, including phage λ DNA (linear dsDNA), M13mp18 ssDNA (circular ssDNA), and synthetic DNA oligonucleotides (linear ssDNA) under the same conditions (Figure S3c-e). We observed that λ DNA and M13mp18 DNA showed similar resistance to cleavage by Exo I and Exo VII as compared with the RCA products, whereas ssDNA oligo was effectively digested by Exo I, Exo III, and Exo VII. Given that in particular DSN has a strong cleavage preference for dsDNA and little activity against ssDNA, both RCA products in solution seemingly have a mixed population of dsDNA and ssDNA, but with a large quantity of dsDNA. This double-stranded configuration can be presumably attributed to random folding of ssDNA due to intramolecular base pairing or bridging between very long, flexible DNA strands. Similar observation has been demonstrated that ssDNA grown on the surface of gold nanoparticles through RCA for 30 min appeared to merge into dsDNA-like structures in some cases.[4,5]

To confirm the results from the nuclease digestion study, we further detected both AmpDNA(-PPase) and AmpDNA(+PPase) with DNA-binding fluorescent dyes, including SYBR Green I, SYBR Green II, and SYBR Gold exhibiting specific detection sensitivity towards ssDNA and dsDNA: *i.e.* SYBR Green I represents an extremely sensitive dye for detecting dsDNA,[6] whereas SYBR Green II shows high sensitivity to detect ssDNA or RNA.[7] SYBR Gold is commonly used

as a universal dye for detecting dsDNA, ssDNA, and RNA with greatly enhanced sensitivity compared to SYBR Green I and SYBR Green II.[8] While these three dyes display binding affinity to ssDNA and dsDNA to some extent, SYBR Green I is well known to show the most pronounced enhancement of fluorescence when bound to dsDNA over ssDNA. To compare the fluorescence intensity of these dyes, serial 2-fold dilutions of DNA samples were incubated with SYBR dyes in parallel, and the fluorescence intensity was recorded. Interestingly, both AmpDNA and λ DNA showed strong fluorescence signals upon the addition of SYBR Green I, while M13mp18 ssDNA exhibited significantly low fluorescence in the presence of SYBR Green I compared to SYBR Green II. These results reveal that there are considerable amounts of dsDNA in AmpDNA regardless of the addition of PPase in the process of RCA.

Table S2. Properties of nucleases used in digestion of AmpDNA.

Enzyme	Polarity	DNA substrate[a)]		Products
		ssDNA	dsDNA	
Exonuclease I (Exo I)[b)]	3' → 5'	+	-	dNMP, dinucleotide
Exonuclease VII (Exo VII) [b)]	3' → 5' 5' → 3'	+	-	Short oligos
Exonuclease III (Exo III) [b)]	3' → 5'	+/-	+	ssDNA, dNMP
Duplex-specific nuclease (DSN) [c)]	5' → 3'	-	+	Short oligos

[a)]Preferred activity on DNA substrate: +, significant activity; -, no significant activity; +/-, greatly reduced activity relative to preferred substrate.
[b)]Referred to the supplier's website: https://www.neb.com/tools-and-resources/selection-charts/properties-of-exonucleases-and-endonucleases
[c)]Referred to the supplier's instructions: http://evrogen.com/protein-descriptions/UM-DSN.pdf
Abbreviations: dNMP, deoxyribonucleoside monophosphate; oligos, oligonucleotides.

Peer reviewed version of the manuscript published in final form at ACS Nano, 2019,
DOI:10.1021/acsnano.8b06492.

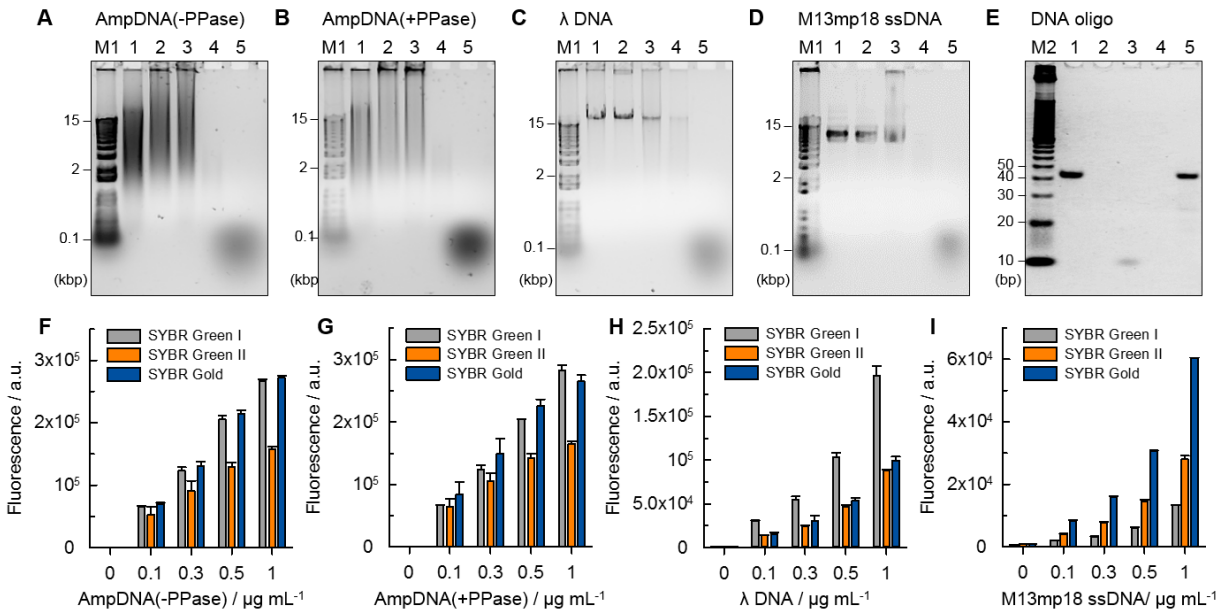

Figure S3. Analysis of the nature of AmpDNA. (A-E) Gel electrophoresis analysis of various DNA after digestion by ssDNA- and/or dsDNA-specific nucleases, including Exo I, Exo VII, Exo III, and DSN: (A) AmpDNA(-PPase), (B) AmpDNA(+PPase), (C) λ DNA, (D) M13mp18 ssDNA, and (E) synthetic ssDNA oligonucleotide. The resulting digested products were analyzed by (A-D) 0.8% agarose gel and (E) 10% native polyacrylamide gel electrophoresis with post-staining using SYBR Gold. Lane M1, 1 kbp DNA marker; lane M2, 10 bp DNA marker; lane 1, non-treated; lane 2, Exo I-treated; lane 3, Exo VII-treated; lane 4, Exo III-treated; lane 5, DSN-treated DNA samples. (F-I) The fluorescence intensity of serial 2-fold dilutions of DNA samples in the presence of dsDNA- and/or ssDNA-specific SYBR dyes (SYBR Green I, SYBR Green II, and SYBR Gold): (F) AmpDNA(-PPase), (G) AmpDNA(+PPase), (H) λ DNA, and (I) M13mp18 ssDNA. The fluorescence was recorded at excitation/emission of 497 nm/520 nm for SYBR Green I and SYBR Green II and 495 nm/537 nm for SYBR Gold, respectively. Data represent mean ± s.d. for three technical replicates.

Peer reviewed version of the manuscript published in final form at ACS Nano, 2019,
DOI:10.1021/acsnano.8b06492.

Note 2. Estimation of Average Repeating Units in AmpDNA. From the gel image, we observed that both AmpDNA, AmpDNA(-PPase) and AmpDNA(+PPase), after EcoRV digestion were converted into two short DNA fragments around 70 and 80 nt, which are similar in size to 75 nt template DNA (Figure S4). It should be noted that the digestion products showed two DNA fragments probably due to variations in size of the AmpDNA as a result of thermal fragmentation (Figure S3a). Using ImageJ software, we compared the intensity of those two DNA bands between 70 and 80 nt to that of 50 nt loading control DNA, and calculated the average repeating units using the following equation: the average repeating unit = (($I_{\text{cleaved AmpDNA}}$ / $I_{\text{loading control}}$) × $\text{mol}_{\text{loading control}}$ × dilution factor) / $\text{mol}_{\text{DNA minicircle}}$, where $I_{\text{cleaved AmpDNA}}$ and $I_{\text{loading control}}$ are the band intensity of cleaved DNA and loading control DNA, and $\text{mol}_{\text{loading control}}$ and $\text{mol}_{\text{DNA minicircle}}$ are 100 and 30 pmol, respectively. The dilution factors were obtained by considering the dilution steps involved in the entire process: *i.e.*, for AmpDNA(-PPase), dilution from 50 μL RCA reaction volume to 100 μL elution volume (100 / 50 = 2) and from 33 ng μL^{-1} to 25 ng μL^{-1} of AmpDNA to hybridize with a primer (33 / 25 = 1.3), and from the volume of 25 ng μL^{-1} AmpDNA used in digestion to the reaction volume of EcoRV digestion (20 / 0.5 = 40). This experiment was performed on three independent samples. As reported in Table S3, the average unit of AmpDNA(+PPase) was estimated to be 298.2 ± 97.8, which was slightly higher than AmpDNA(-PPase) (247.4 ± 28.5).

Peer reviewed version of the manuscript published in final form at ACS Nano, 2019,
DOI:10.1021/acsnano.8b06492.

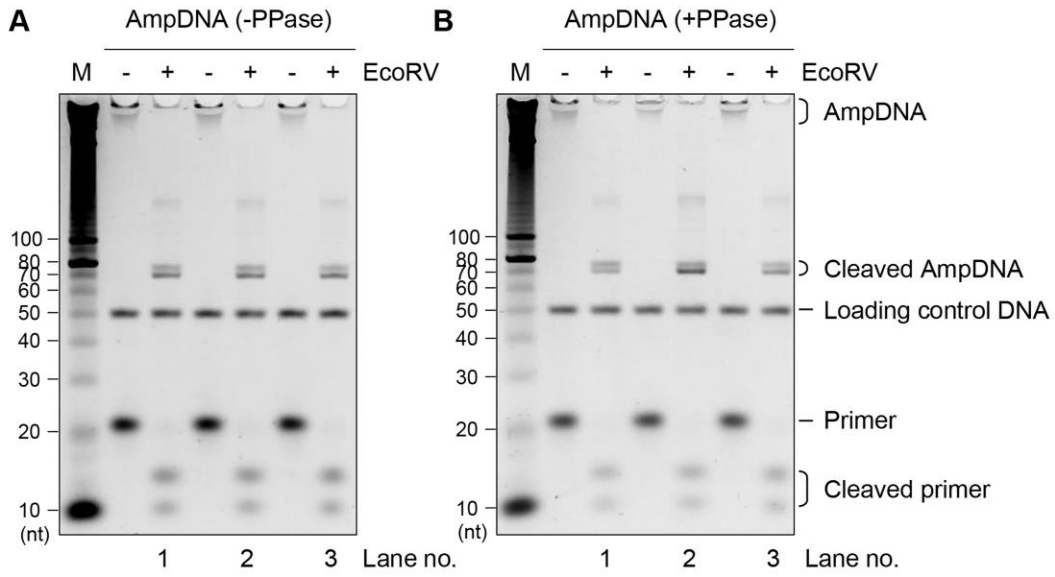

Figure S4. Digestion of AmpDNA by EcoRV restriction endonuclease. The AmpDNA synthesized by RCA in the (A) absence (AmpDNA(-PPase)) and (B) presence of PPase (AmpDNA(+PPase)) in triplicate were digested by EcoRV with the aid of the primer and analyzed by 10% denaturing polyacrylamide gel electrophoresis with post-staining using SYBR Gold. Non-treated AmpDNA was also run as a reference. The 50 nt DNA was co-loaded with samples as a loading control (1 pmol per lane). Lane M, 10 nt DNA marker. The band intensity of the cleaved AmpDNA around 70 to 80 nt and the loading control DNA positioned at 50 nt in lane 1-3 was used to calculate the average repeating units of AmpDNA.

Table S3. Estimation of average repeating units in AmpDNA.

Sample	Lane no.	$I_{cleaved\ AmpDNA}$	$I_{loading\ control}$	$pmol_{loading\ control}$	Dilution factor	$pmol_{DNA\ minicircle}$	Repeating unit	Avg. repeating unit
AmpDNA (-PPase)	1	6216.2	8255.2	100	106.9	30	268.3	247.4 ± 28.5
	2	6328.8	7817.8	100	96.0	30	259.1	
	3	5695.3	8650.1	100	97.9	30	214.9	
AmpDNA (+PPase)	1	5092.1	8286.5	100	99.2	30	203.2	298.2 ± 97.8
	2	9314.3	8127.8	100	104.3	30	398.5	
	3	5571.7	7976.8	100	125.8	30	292.8	

Peer reviewed version of the manuscript published in final form at ACS Nano, 2019,
DOI:10.1021/acsnano.8b06492.

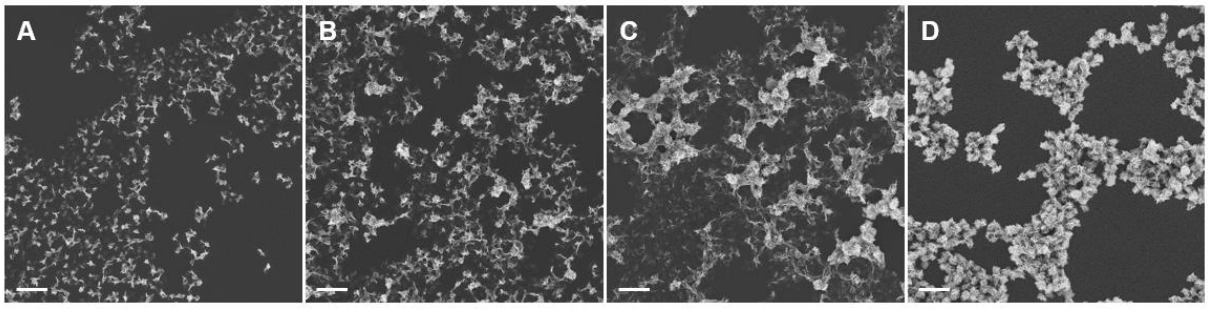

Figure S5. Time-dependent crystallization of Mg_2PPi in the presence of AmpDNA. Representative SE-SEM images of Mg_2PPi/AmpDNA at various time intervals: (A) 1 h, (B) 2 h, (C) 10 h, and (D) 20 h. Scale bar, 2 μm.

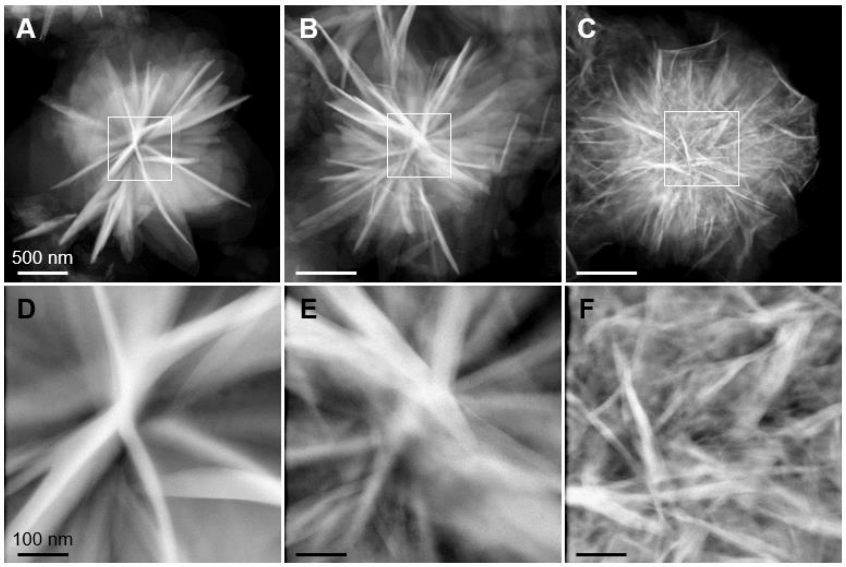

Figure S6. Representative HAADF-STEM images of a single Mg_2PPi particle precipitated with different concentrations of PPi ions: (A, D) 0.5 mM, (B, E) 1 mM, and (C, F) 2 mM. (D-F) High-magnification images indicate HAADF-STEM images of the area marked in the solid line. Scale bars, 500 nm (A-C) and 100 nm (D-F).

Peer reviewed version of the manuscript published in final form at ACS Nano, 2019,
DOI:10.1021/acsnano.8b06492.

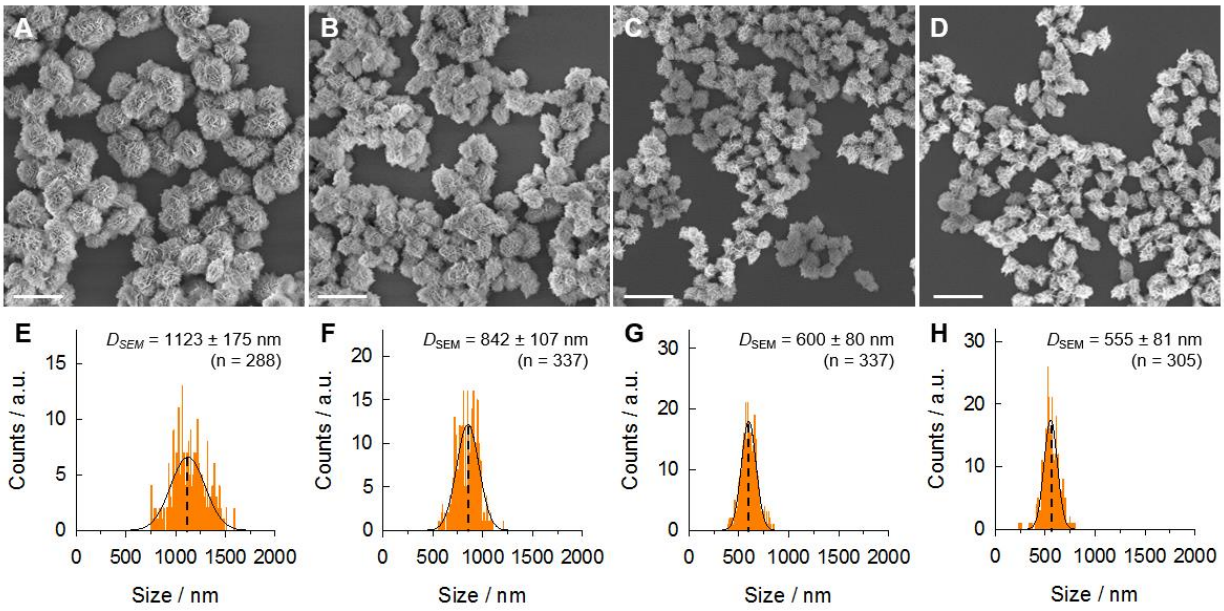

Figure S7. Representative (A-D) SE-SEM images and (E-H) size distribution of Mg_2PPi particles grown with the addition of an increasing amount of AmpDNA: (A) 13 μg mL^{-1}, (B) 27 μg mL^{-1}, (C) 40 μg mL^{-1}, and (D) 67 μg mL^{-1}. The size distribution was determined from SEM images, fitted into the Gaussian distribution. In (E-H), the insets represent mean ± s.d. of the size analysis over about 280−340 particles per sample. Scale bar, 2 μm.

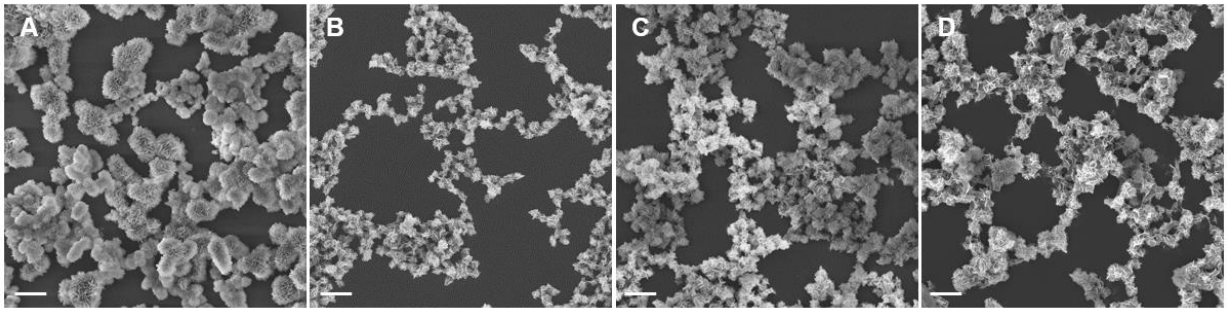

Figure S8. The effects of various types of DNA on formation of Mg_2PPi/DNA composites. Representative SE-SEM images of Mg_2PPi particles prepared (A) without and (B-D) with DNA (40 μg mL^{-1}), including (B) AmpDNA, (C) λ DNA, and (D) M13mp18 ssDNA, respectively. Scale bar, 2 μm.

Peer reviewed version of the manuscript published in final form at ACS Nano, 2019,
DOI:10.1021/acsnano.8b06492.

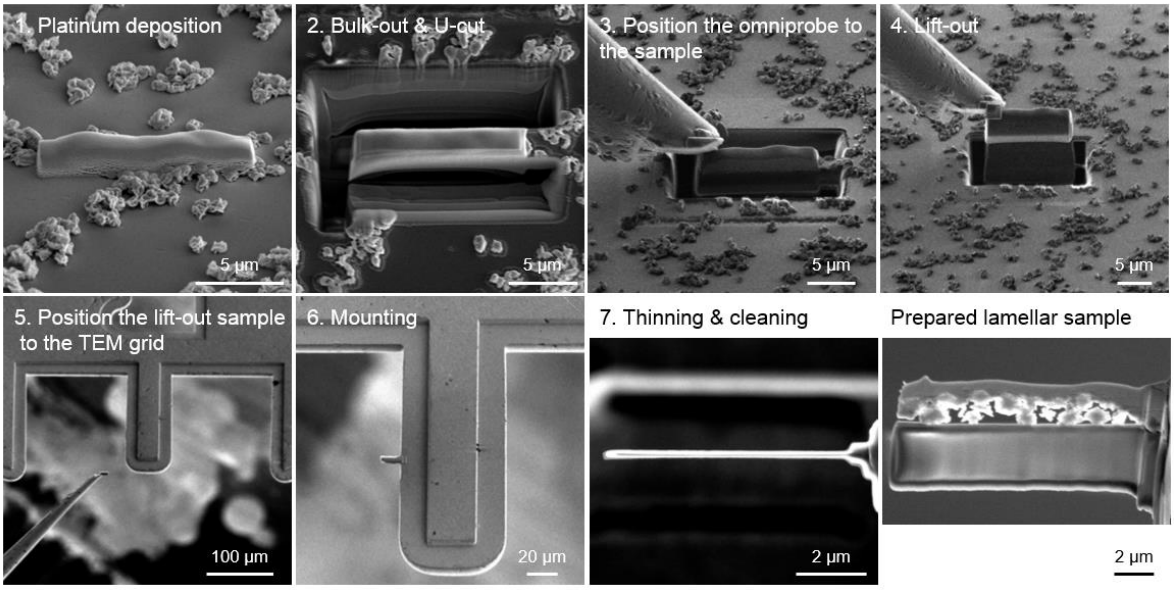

Figure S9. Site-specific preparation of the lamellar specimen for STEM-EELS analysis using the FIB lift-out technique.

Peer reviewed version of the manuscript published in final form at ACS Nano, 2019,
DOI:10.1021/acsnano.8b06492.

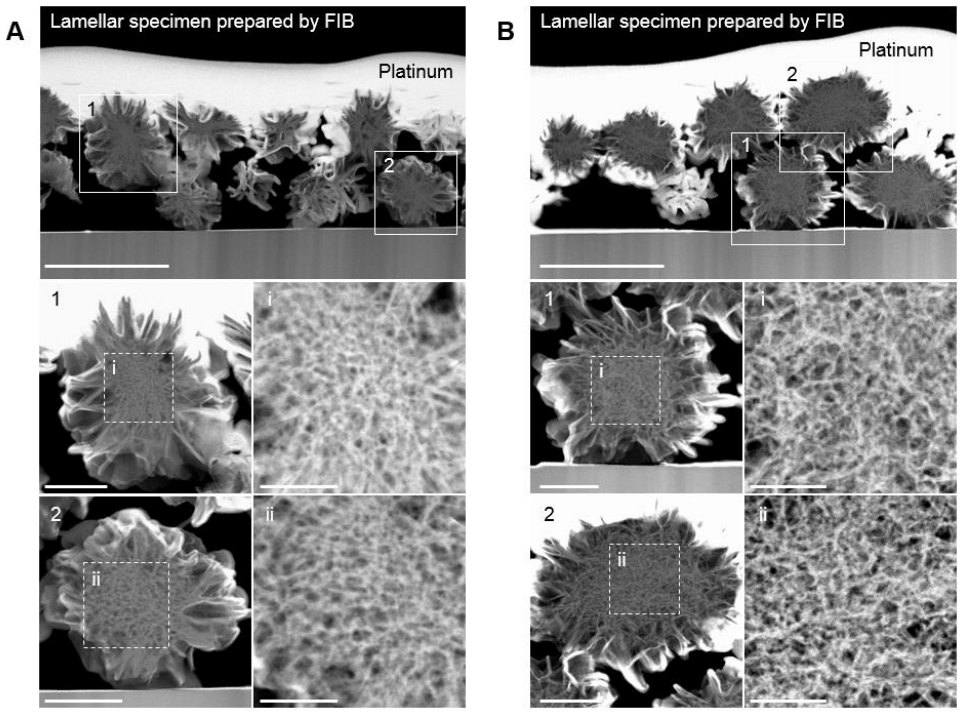

Figure S10. HAADF-STEM images of the lamellar specimens prepared by the FIB at different magnifications: (A) Mg_2PPi/AmpDNA-R and (B) DNF-R. The particles numbered 1 and 2 marked in (A) and (B) were further analysed by STEM-EELS. The obtained EELS elemental maps and spectra of the particle numbered 1 were shown in Figure 5. Scale bars, 2 μm (top), 500 nm (bottom left), 200 nm (bottom right) in (A) and (B).

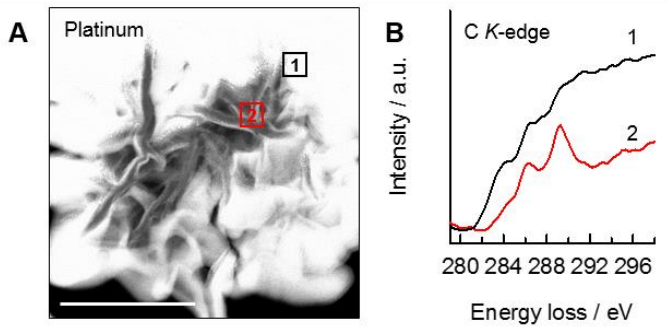

Figure S11. EELS reference spectrum from the platinum region. (A) HAADF-STEM image of the DNF lamellar sample and (B) EELS C *K*-edge spectra from the platinum-coated region (1) and within the sample (2), as indicated in (A). Scale bar, 500 nm.

Peer reviewed version of the manuscript published in final form at ACS Nano, 2019,
DOI:10.1021/acsnano.8b06492.

Note 3. SIM Imaging of Protein-Entrapped Mg_2PPi/AmpDNA. We obtained additional evidence of protein encapsulation using the super-resolution structured illumination microscopy (SIM) technique, which can achieve an enhanced spatial resolution of ~100 nm in the lateral directions and simultaneous multicolor imaging with conventional fluorophores.[9] For SIM imaging, we prepared fluorescent AmpDNA by direct enzymatic incorporation of Cy3-modified deoxynucleotides (dNTPs) during RCA, followed by subsequent isolation with ethanol precipitation. We also coupled RNase A with N-hydroxysuccinimide fluorescein before precipitation with Mg_2PPi. For comparison, we synthesized fluorescent DNF and DNF-R by performing RCA with Cy3-labeled dNTPs and a fluorescein-labeled enzyme. We then collected 3D SIM z-stacks of each particle, in which DNA or enzymes could be identified as fluorescent signals inside the particles (Figure S12). Consistent with DNF, the cross-sections of Mg_2PPi/AmpDNA composites were homogeneously fluorescent. More interestingly, the enzyme encapsulation in Mg_2PPi showed distinct localization compared to DNA-associated particles, where RNase A was predominantly located on the periphery of the surface of Mg_2PPi without DNA, while it was evenly distributed in the entire region of Mg_2PPi/AmpDNA or DNF. This result can be attributed to the presence of DNA molecules that impede the rapid growth of crystals and electrostatically interact with positively charged RNase A. This leads to trapping of proteins into the hydrated polymer-like DNA network throughout particles, not only at their surfaces.

Peer reviewed version of the manuscript published in final form at ACS Nano, 2019,
DOI:10.1021/acsnano.8b06492.

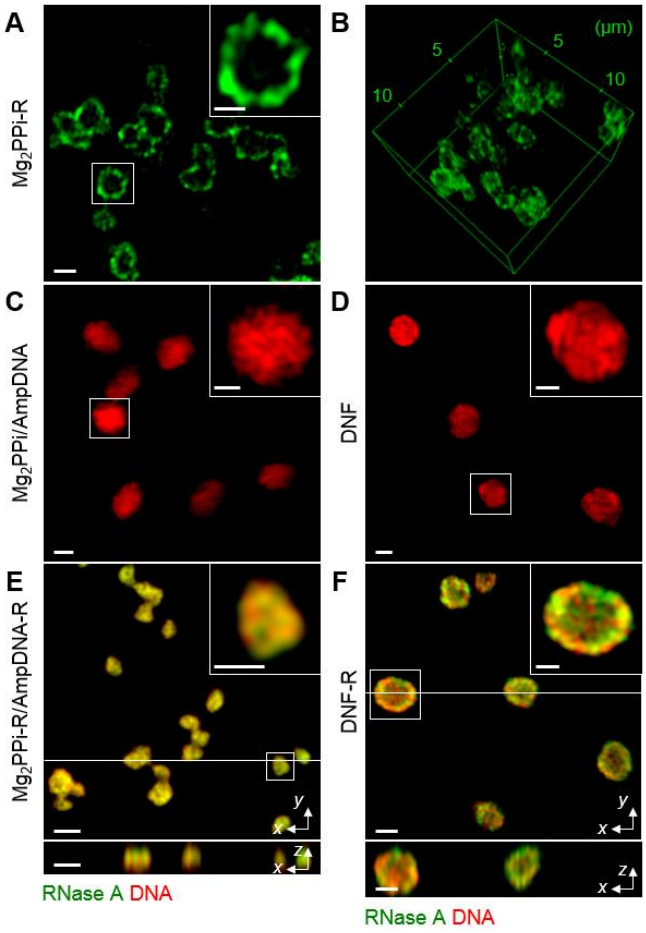

Figure S12. 3D SIM imaging of DNA- and/or enzyme-incorporated Mg_2PPi composites. (A) 2D cross-sectional and (B) 3D reconstructed images of Mg_2PPi-R, cross sections of (C) Mg_2PPi-R/AmpDNA, (D) DNF, (E) Mg_2PPi/AmpDNA-R, and (F) DNF-R. In (E) and (F), orthogonal cross sections were also shown. RNase A and DNA were labeled with fluorescein (green) and Cy3 (red), respectively. Insets indicate higher magnification views of the region marked by the white box in the main image. Scale bars, 1 μm (main panels) and 0.5 μm (inset panels).

Peer reviewed version of the manuscript published in final form at ACS Nano, 2019,
DOI:10.1021/acsnano.8b06492.

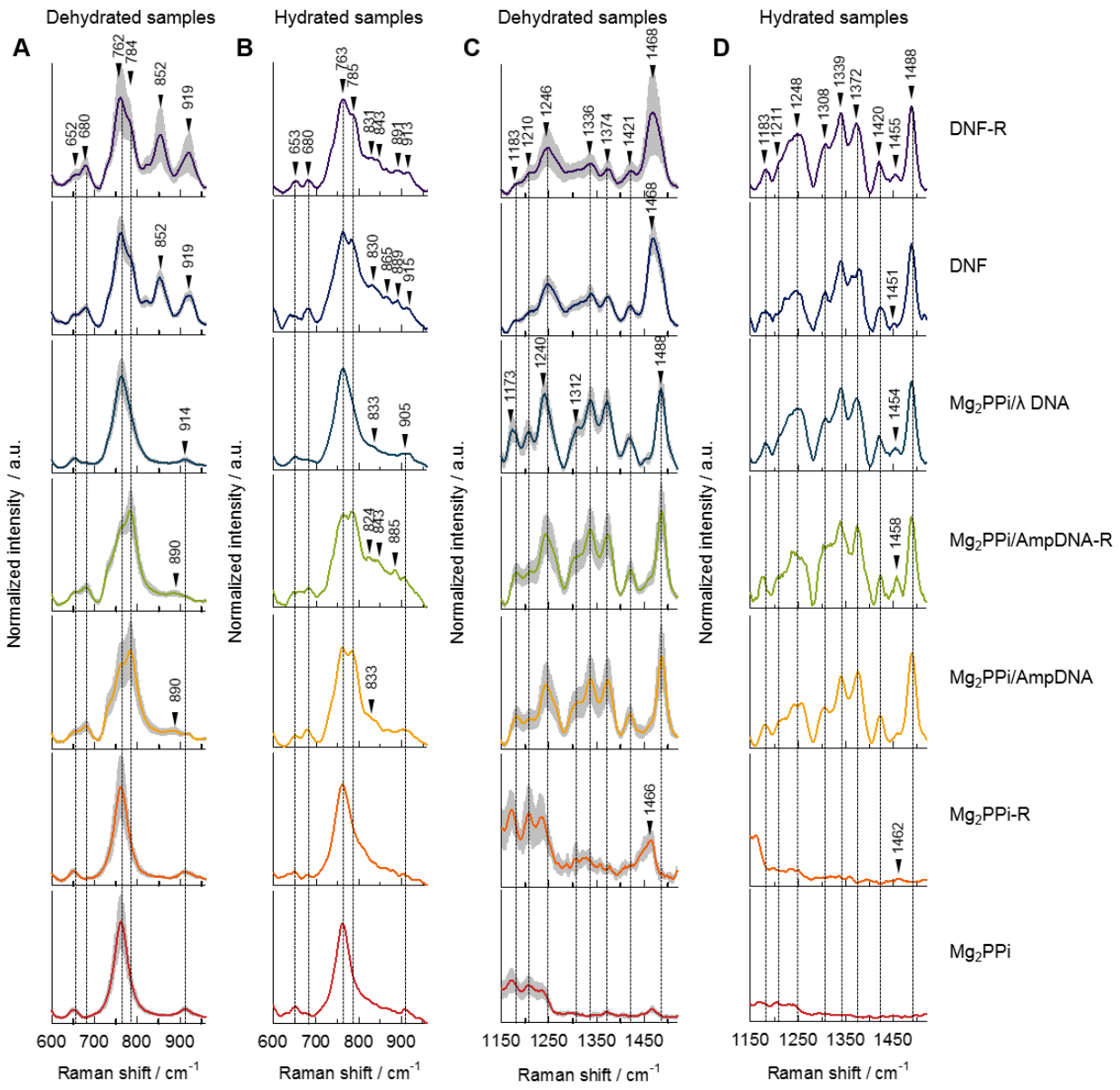

Figure S13. Comparison of Raman spectra over the range of (A, B) 600−920 cm^{-1} and (C, D) 1150−1520 cm^{-1} for each Mg_2PPi composite prepared by a co-precipitation method or a one-pot RCA process. For Raman measurements, (A, C) the solid films prepared by evaporation of aqueous sample solution and (B, D) droplets of aqueous solution samples on a calcium fluoride substrate were used. The spectra in (A) and (C) show the average spectra ± s.d. of five different points randomly selected in the sample. The spectra in (B) and (D) show representative spectra of one point in the sample.

Peer reviewed version of the manuscript published in final form at ACS Nano, 2019,
DOI:10.1021/acsnano.8b06492.

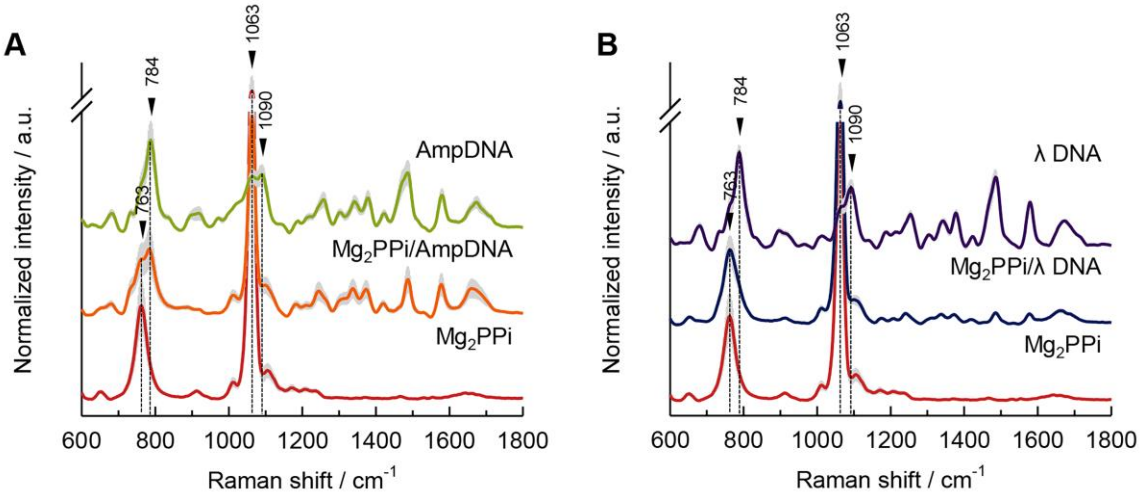

Figure S14. Raman spectra of (A) Mg_2PPi, Mg_2PPi/AmpDNA, and AmpDNA, and (B) Mg_2PPi, Mg_2PPi/λ DNA, and λ DNA, prepared by evaporation of aqueous sample solution. The spectra show the average spectra ± s.d. of five different points randomly selected in the sample .

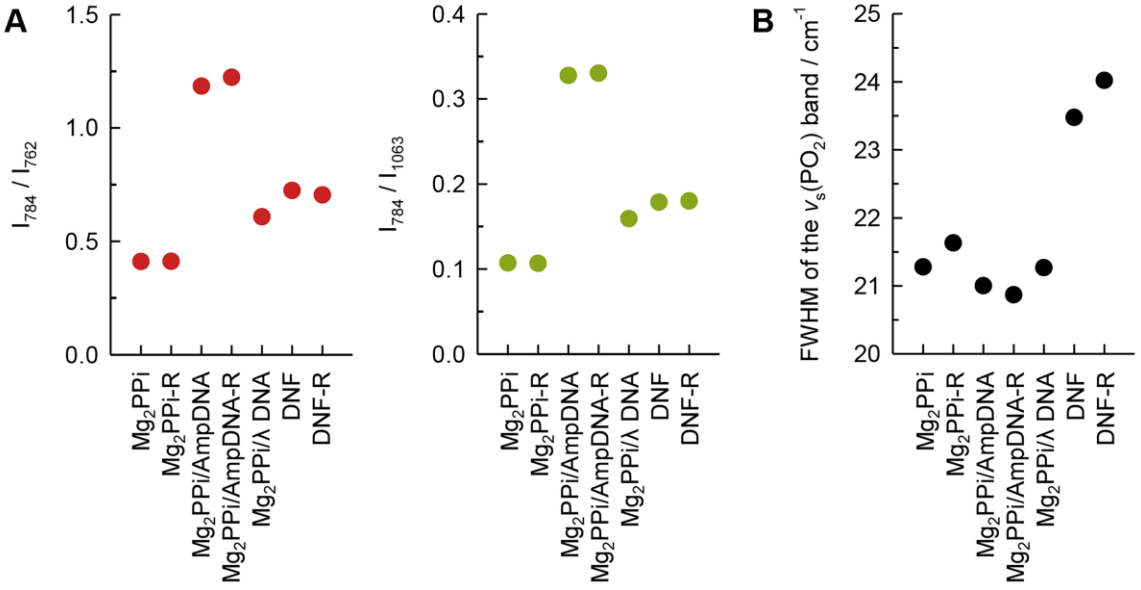

Figure S15. (A) Intensity ratio of the signals for the ν_s(OPO) band at 784 cm^{-1}, the ν_s(POP) at 762 cm^{-1}, and the $\nu_s(PO_2)$ band at 1063 cm^{-1}, and (B) FWHM of the $\nu_s(PO_2)$ band centered at 1063 cm^{-1} for different Mg_2PPi composites.

Peer reviewed version of the manuscript published in final form at ACS Nano, 2019, DOI:10.1021/acsnano.8b06492.

Table S4. Tentative Raman band assignment of various Mg_2PPi composites measured in dehydrated forms.

Mg_2PPi	Mg_2PPi-R	Mg_2PPi/AmpDNA	Mg_2PPi/AmpDNA-R	Mg_2PPi/λ DNA	DNF	DNF-R	AmpDNA	λ DNA	Assignment[a)]
		680	680	681	678	678	682	680	dG
763	763	763	762	763	763	762			ν_s(POP)
		784	784		783	783	786	788	ν_s(OPO)
							833	833	ν_s(OPO)
					853	855			Tyr
		890	887	887					Deoxy
912	910	918	918	912			914	908	ν_{as}(POP)
					920	920			Glu
1013	1011	1013	1011	1013	1011	1011	1020	1017	$\nu_s(PO_3)$
1063	1063	1063	1063	1063	1062	1062	1063	1068	$\nu_s(PO_2)$
1105	1103	1100	1100	1102	1100	1100	1090	1092	$\nu_s(PO_2)$
1172	1172								$\nu_{as}(PO_3)$
							1141	1137	Deoxy
		1182	1182	1176	1182	1188	1186	1188	dT
1206	1208	1211	1212	1206	1212	1212	1218	1218	$\nu_{as}(PO_2)$
1237	1236								$\nu_{as}(PO_2)$
		1245	1243	1241	1247	1247	1255	1255	dC, dT
		1308	1310	1312	1310	1314	1302	1304	dA, dC
		1338	1336	1338	1338	1336	1344	1342	dA, dG
		1373	1373	1373	1373	1373	1377	1377	dT
		1420	1420	1420	1420	1423	1423	1423	2' CH_2
	1464				1470	1468			Ala
		1488	1488	1486			1486	1486	dA, dG
		1578	1578	1578	1578	1578	1580	1580	dA, dG
		1661	1665	1663	1663	1669	1673	1671	dT

[a)]Abbreviations: ν_s, symmetric stretching; ν_{as}, asymmetric stretching; δ, bending; POP, POP bridge; OPO, phosphodiester backbone; PO_2 or PO_3, anionic phosphate group; Deoxy, Deoxyribose; dA, deoxyadenine; dC, deoxycytosine; dG, deoxyguanine; dT, deoxythymine; Tyr, Tyrosine; Glu, Glutamic acid; Ala, Alanine.

Peer reviewed version of the manuscript published in final form at ACS Nano, 2019, DOI:10.1021/acsnano.8b06492.

Table S5. Tentative Raman assignment of various Mg_2PPi composites measured in hydrated forms.

Mg_2PPi	Mg_2PPi-R	Mg_2PPi/ AmpDNA	Mg_2PPi/ AmpDNA-R	Mg_2PPi/ λ DNA	DNF	DNF-R	Assignment[a)]
		680	684	673	681	681	dG
763	763	763	767	763	764	764	v_s(POP)
		784	784		782	785	v_s(OPO)
		832	831	834	831	831	v_s(OPO)
			842		862	842	Tyr
		867	887		891	891	Deoxy
908	905	902	906	909	914	914	v_{as}(POP)
			969				Glu
1013	995	1011	1007	1012	1012	1010	$v_s(PO_3)$
1062	1062	1062	1062	1062	1062	1062	$v_s(PO_2)$
1109	1111	1093	1094	1097	1092	1095	$v_s(PO_2)$
1168	1160						$v_{as}(PO_3)$
		1180	1176	1175	1180	1183	dT
1206	1198	1218	1212	1209	1209	1211	$v_{as}(PO_2)$
1237	1237						$v_{as}(PO_2)$
		1241	1241	1240	1249	1248	dC, dT
		1306	1306	1307	1307	1307	dA, dC
		1340	1338	1338	1341	1341	dA, dG
		1375	1375	1377	1379	1372	dT
		1424	1422	1421	1423	1421	2' CH_2
			1458		1454	1454	dT
		1489	1489	1488	1488	1488	dA, dG
		1580	1586	1584	1581	1584	dA, dG
1643	1643	1653	1653	1650	1650	1648	δH_2O
		1660	1663	1664	1664	1664	dT

[a)]Abbreviations: v_s, symmetric stretching; v_{as}, asymmetric stretching; δ, bending; POP, POP bridge; OPO, phosphodiester backbone; PO_2 or PO_3, anionic phosphate group; Deoxy, Deoxyribose; dA, deoxyadenine; dC, deoxycytosine; dG, deoxyguanine; dT, deoxythymine; Tyr, Tyrosine; Glu, Glutamic acid; Ala, Alanine.

Peer reviewed version of the manuscript published in final form at ACS Nano, 2019, DOI:10.1021/acsnano.8b06492.

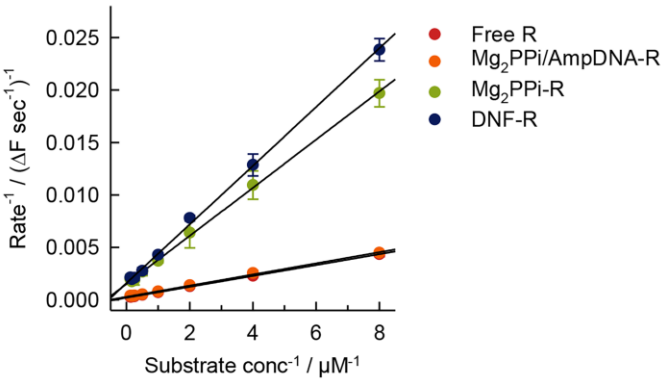

Figure S16. Lineweaver-Burk plot of free RNase A (R), Mg_2PPi/AmpDNA-R, Mg_2PPi-R, and DNF-R. The concentration of RNase A in each sample was 0.5 ng mL^{-1}. Results represent mean ± s.d. for four independent experiments.

Table S6. Enzyme kinetics showing the Michaelis-Menten constant (K_m) and maximum velocity (V_{max}) of free enzyme and the encapsulated enzyme in Mg_2PPi/AmpDNA, Mg_2PPi, and DNF. Data represent mean ± s.d. for four independent experiments.

Sample	K_m / μM	V_{max} / ΔF sec^{-1}
Free RNase A	2.5 ± 0.2	4913.2 ± 187.1
Mg_2PPi/AmpDNA-R	1.8 ± 0.03	3460.4 ± 119.3
Mg_2PPi-R	1.5 ± 0.1	668.4 ± 83.9
DNF-R	1.8 ± 0.1	628.7 ± 49.5

Peer reviewed version of the manuscript published in final form at ACS Nano, 2019, DOI:10.1021/acsnano.8b06492.

References

(1) Hermanowicz, P.; Sarna, M.; Burda, K.; Gabryś, H. AtomicJ: An Open Source Software for Analysis of Force Curves. *Rev. Sci. Instrum.* **2014**, *85*, 063703.

(2) Liu, M.; Hui, C. Y.; Zhang, Q.; Gu, J.; Kannan, B.; Jahanshahi-Anbuhi, S.; Filipe, C. D. M.; Brennan, J. D.; Li, Y. Target-Induced and Equipment-Free DNA Amplification with a Simple Paper Device. *Angew. Chem. Int. Ed.* **2016**, *55*, 2709-2713.

(3) Liu, M.; Zhang, Q.; Kannan, B.; Botton, G. A.; Yang, J.; Soleymani, L.; Brennan, J. D.; Li, Y. Self-Assembled Functional DNA Superstructures as High-Density and Versatile Recognition Elements for Printed Paper Sensors. *Angew. Chem. Int. Ed.* **2018**, *57*, 12440-12443.

(4) Zhao, W.; Gao, Y.; Kandadai, S. A.; Brook, M. A.; Li, Y. DNA Polymerization on Gold Nanoparticles Through Rolling Circle Amplification: Towards Novel Scaffolds for Three-Dimensional Periodic Nanoassemblies. *Angew. Chem. Int. Ed.* **2006**, *45*, 2409-2413.

(5) Yan, J.; Hu, C.; Wang, P.; Zhao, B.; Ouyang, X.; Zhou, J.; Liu, R.; He, D.; Fan, C.; Song, S. Growth and Origami Folding of DNA on Nanoparticles for High-Efficiency Molecular Transport in Cellular Imaging and Drug Delivery. *Angew. Chem. Int. Ed.* **2015**, *54*, 2431-2435.

(6) Zipper, H.; Brunner, H.; Bernhagen, J.; Vitzthum, F. Investigations on DNA Intercalation and Surface Binding by SYBR Green I, Its Structure Determination and Methodological Implications. *Nucleic Acids Res.* **2004**, *32*, e103.

(7) Lee, L. G.; Chen, C.-H.; Chiu, L. A. Thiazole Orange: A New Dye for Reticulocyte Analysis. *Cytometry* **1986**, *7*, 508-517.

(8) Tuma, R. S.; Beaudet, M. P.; Jin, X.; Jones, L. J.; Cheung, C.-Y.; Yue, S.; Singer, V. L. Characterization of SYBR Gold Nucleic Acid Gel Stain: A Dye Optimized for Use with 300-nm Ultraviolet Transilluminators. *Anal. Biochem.* **1999**, *268*, 278-288.

(9) Huang, B.; Babcock, H.; Zhuang, X. Breaking the Diffraction Barrier: Super-Resolution Imaging of Cells. *Cell* **2010**, *143*, 1047-1058.